

Approximating and Preconditioning the Stiffness Matrix in the GoFD Approximation of the Fractional Laplacian

Weizhang Huang¹ and Jinye Shen^{2,*}

¹ Department of Mathematics, University of Kansas, Lawrence, Kansas, U.S.A.

² School of Mathematics, Southwestern University of Finance and Economics, Chengdu, P.R. China.

Received 4 April 2024; Accepted (in revised version) 11 July 2024

Abstract. In the finite difference approximation of the fractional Laplacian the stiffness matrix is typically dense and needs to be approximated numerically. The effect of the accuracy in approximating the stiffness matrix on the accuracy in the whole computation is analyzed and shown to be significant. Four such approximations are discussed. While they are shown to work well with the recently developed grid-over finite difference method (GoFD) for the numerical solution of boundary value problems of the fractional Laplacian, they differ in accuracy, economics to compute, performance of preconditioning, and asymptotic decay away from the diagonal line. In addition, two preconditioners based on sparse and circulant matrices are discussed for the iterative solution of linear systems associated with the stiffness matrix. Numerical results in two and three dimensions are presented.

AMS subject classifications: 65N06, 35R11

Key words: Fractional Laplacian, finite difference approximation, stiffness matrix, preconditioning, overlay grid.

1 Introduction

We are concerned with the finite difference (FD) solution of the boundary value problem (BVP) of the fractional Laplacian,

$$\begin{cases} (-\Delta)^s u = f, & \text{in } \Omega, \\ u = 0, & \text{in } \Omega^c, \end{cases} \quad (1.1)$$

*Corresponding author. Email addresses: jyshen@swufe.edu.cn (J. Shen), whuang@ku.edu (W. Huang)

where $(-\Delta)^s$ is the fractional Laplacian with the fractional order $s \in (0,1)$, Ω is a bounded domain in \mathbb{R}^d ($d \geq 1$), $\Omega^c \equiv \mathbb{R}^d \setminus \Omega$ is the complement of Ω , and f is a given function. The fractional Laplacian can be expressed in the singular integral form as

$$(-\Delta)^s u(\vec{x}) = \frac{2^{2s} s \Gamma(s + \frac{d}{2})}{\pi^{\frac{d}{2}} \Gamma(1-s)} \text{p.v.} \int_{\mathbb{R}^d} \frac{u(\vec{x}) - u(\vec{y})}{|\vec{x} - \vec{y}|^{d+2s}} d\vec{y}, \quad (1.2)$$

or in terms of the Fourier transform as

$$(-\Delta)^s u = \mathcal{F}^{-1}(|\vec{\xi}|^{2s} \mathcal{F}(u)), \quad (1.3)$$

where p.v. stands for the Cauchy principal value, $\Gamma(\cdot)$ is the gamma function, and \mathcal{F} and \mathcal{F}^{-1} denote the Fourier and inverse Fourier transforms, respectively. When Ω is a simple domain such as a rectangle or a cube, BVP (1.1) can be solved using finite differences on a uniform grid (see, e.g., [26,28]). When Ω is an arbitrary bounded domain (including a simple domain), BVP (1.1) can be solved using the recently developed grid-overlay finite difference (GoFD) method with a simplicial mesh [28] or a point cloud [40]. Generally speaking, the stiffness matrix in FD approximations is dense and needs to be approximated numerically. The effect of the accuracy in the approximation on the accuracy in the numerical solution of BVP (1.1) has not been studied in the past. A main objective of the present work is to study this important issue for the numerical approximation of the fractional Laplacian. It will be shown that the effect is actually significant. As a result, it is necessary to develop accurate and reasonably economic approximations for the stiffness matrix. We will study four approximations. The first two are based on the fast Fourier transform (FFT) with uniform and non-uniform sampling points. The third one is the spectral approximation of Zhou and Zhang [47]. We will discuss a new and fast implementation of this approximation and derive the asymptotic decay rate of its entries away from the diagonal line. The last one is a modification of the spectral approximation. Properties of these approximations are summarized in Table 3. In addition, we will study two preconditioners based on sparse and circulant matrices for the iterative solution of linear systems associated with the stiffness matrix.

For the purpose of numerical verification and demonstration, we consider an example of BVP (1.1) with the analytical exact solution (cf. [21, Theorem 3]),

$$\Omega = B_1(0), \quad f = 1, \quad u = \frac{\Gamma(\frac{d}{2})}{2^{2s} \Gamma(1+s) \Gamma(\frac{d}{2} + s)} (1 - |\vec{x}|^2)_+^s, \quad (1.4)$$

where $B_1(0)$ is the unit ball centered at the origin. Numerical results will be given in two and three dimensions.

The fractional Laplacian is a fundamental non-local operator in the modeling of anomalous dynamics; see, for example, [6,31,33] and references therein. A number of numerical methods have been developed, including FD methods [16,18,19,26,30,31,34,37,43,45,46], finite element methods [1-4, 10, 11, 22, 44], spectral methods [32, 41, 47], discontinuous

Galerkin methods [17], meshfree methods [12,36], neural network method [25], and sinc-based methods [7]. Loosely speaking, methods such as FD methods are constructed on uniform grids and have the advantage of efficient matrix-vector multiplication via FFT but do not work for complex domains and with mesh adaptation. On the other hand, methods such as finite element methods can work for arbitrary bounded domains and with mesh adaptation but suffer from slowness of stiffness matrix assembling and matrix-vector multiplication because the stiffness matrix is dense. Few methods can do both. A sparse approximation to the stiffness matrix of finite element methods and an efficient multigrid implementation have been proposed by Ainsworth and Glusa [3,4]. The GoFD method of [28, 40] is an FD method that uses FFT for fast computation and works for arbitrary bounded domains with unstructured meshes or point clouds. Anisotropic non-local diffusion models and inhomogeneous fractional Dirichlet problem are also studied in [15,42].

An outline of the present paper is as follows. The GoFD method and uniform-grid FD approximation of the fractional Laplacian are described in Sections 2 and 3, respectively. The effect of the accuracy in the approximation of the stiffness matrix on the accuracy in the numerical solution of BVP (1.1) is analyzed in Section 4 while four approximations to the stiffness matrix are discussed in Section 5. Section 6 is devoted to the study of two preconditioners, a sparse preconditioner and a circulant preconditioner, for iteratively solving linear systems associated with the stiffness matrix. Numerical results in two and three dimensions are presented in Section 7. Finally, conclusions are drawn in Section 8.

2 The grid-overlay FD method

To describe the GoFD method [28] for the numerical solution of BVP (1.1), we assume that an unstructured simplicial mesh \mathcal{T}_h is given for Ω . Denote its vertices by $\vec{x}_1, \dots, \vec{x}_{N_{vi}}, \dots, \vec{x}_{N_v}$, where N_v and N_{vi} are the numbers of the vertices and interior vertices, respectively. Here, the vertices are arranged so that the interior vertices are listed before the boundary ones. We also assume that a d -dimensional cube, $\Omega_{\text{FD}} \equiv (-R_{\text{FD}}, R_{\text{FD}})^d$, has been chosen to contain Ω . For a given positive integer N_{FD} , let \mathcal{T}_{FD} be a uniform grid for Ω_{FD} with $2N_{\text{FD}} + 1$ nodes in each axial direction. The spacing of \mathcal{T}_{FD} is given by

$$h_{\text{FD}} = \frac{R_{\text{FD}}}{N_{\text{FD}}}. \quad (2.1)$$

Denote the vertices of \mathcal{T}_{FD} by $\vec{x}_k^{\text{FD}}, k = 1, \dots, N_v^{\text{FD}}$. Then, a uniform-grid FD approximation, denoted by $h_{\text{FD}}^{-2s} A_{\text{FD}}$, can be developed for the fractional Laplacian on \mathcal{T}_{FD} ; cf. Section 3. It is known [28] that A_{FD} is symmetric and positive definite. The GoFD approximation of BVP (1.1) is then defined as

$$A_h \vec{u}_h = \vec{f}_h, \quad A_h \equiv \frac{1}{h_{\text{FD}}^{2s}} D_h^{-1} (I_h^{\text{FD}})^T A_{\text{FD}} I_h^{\text{FD}}, \quad (2.2)$$

where $\vec{u}_h = (u_1, \dots, u_{N_{vi}})^T$ is an FD approximation of u , $\vec{f}_h = (f(\vec{x}_1), \dots, f(\vec{x}_{N_{vi}}))^T$, I_h^{FD} is a transfer matrix from the mesh \mathcal{T}_h to the uniform grid \mathcal{T}_{FD} , and D_h is the diagonal matrix formed by the column sums of I_h^{FD} . The invertibility of D_h will be addressed in Theorem 2.1 below. Rewrite A_h as

$$A_h = \frac{1}{h_{\text{FD}}^{2s}} D_h^{-\frac{1}{2}} \cdot (I_h^{\text{FD}} D_h^{-\frac{1}{2}})^T A_{\text{FD}} (I_h^{\text{FD}} D_h^{-\frac{1}{2}}) \cdot D_h^{\frac{1}{2}}.$$

Thus, A_h is similar to the symmetric and positive semi-definite matrix

$$\frac{1}{h_{\text{FD}}^{2s}} (I_h^{\text{FD}} D_h^{-\frac{1}{2}})^T A_{\text{FD}} (I_h^{\text{FD}} D_h^{-\frac{1}{2}}),$$

which can be shown to be positive definite when I_h^{FD} is of full column rank. Notice that D_h^{-1} is included in (2.2) to ensure that the row sums of $D_h^{-1} (I_h^{\text{FD}})^T$ be equal to one. As a consequence, $D_h^{-1} (I_h^{\text{FD}})^T$ represents a data transfer from \mathcal{T}_{FD} to \mathcal{T}_h and preserves constant functions.

We now consider a special choice of I_h^{FD} as linear interpolation. For any function $u(\vec{x})$, we can express its piecewise linear interpolant as

$$I_h u(\vec{x}) = \sum_{j=1}^{N_v} u_j \phi_j(\vec{x}), \quad (2.3)$$

where $u_j = u(\vec{x}_j)$ and ϕ_j is the Lagrange-type linear basis function associated with vertex \vec{x}_j . (The basis function ϕ_j is considered to be zero outside the domain Ω , i.e., $\phi_j|_{\Omega^c} = 0$.) Then,

$$I_h u(\vec{x}_k^{\text{FD}}) = \sum_{j=1}^{N_v} u_j \phi_j(\vec{x}_k^{\text{FD}}), \quad k = 1, \dots, N_v^{\text{FD}}$$

which gives rise to

$$(I_h^{\text{FD}})_{k,j} = \phi_j(\vec{x}_k^{\text{FD}}), \quad k = 1, \dots, N_v^{\text{FD}}, \quad j = 1, \dots, N_v. \quad (2.4)$$

Theorem 2.1 ([28]). *Assume that N_{FD} is taken sufficiently large such that*

$$h_{\text{FD}} \leq \frac{a_h}{(d+1)\sqrt{d}}, \quad (2.5)$$

where a_h is the minimum element height of \mathcal{T}_h . Then, the transfer matrix I_h^{FD} associated with piecewise linear interpolation is of full column rank. As a result, D_h is invertible and the GoFD stiffness matrix given in (2.2) for the fractional Laplacian is similar to a symmetric and positive definite matrix and thus invertible.

The sufficient condition (2.5) for the invertibility of A_h is conservative in general. Numerical experiment suggests that a less restrictive condition, such as

$$h_{\text{FD}} \leq a_h, \quad (2.6)$$

can be used in practical computation.

The linear algebraic system (2.2) can be rewritten as

$$(I_h^{\text{FD}})^T A_{\text{FD}} I_h^{\text{FD}} \vec{u}_h = h_{\text{FD}}^{2s} D_h \vec{f}_h. \quad (2.7)$$

While I_h^{FD} is sparse, A_{FD} is dense and needs to be approximated numerically in multi-dimensions (cf. Section 3). Unfortunately, this has a consequence that the accuracy of approximating A_{FD} can have a significant impact on the accuracy in the FD solution of BVP (1.1). This impact will be analyzed in Section 4. Moreover, several approaches for approximating the stiffness matrix will be discussed in Section 5.

It is worth pointing out that although the coefficient matrix of (2.7) is dense, its multiplication with vectors can be carried out efficiently using FFT (cf. Section 3). Therefore, it is practical to use an iterative method for solving (2.7). In our computation, we use the preconditioned conjugate gradient (PCG) method since the coefficient matrix is symmetric and positive definite when the transfer matrix is of full column rank. Preconditioning will be discussed in Section 6.

3 The uniform-grid FD approximation of the fractional Laplacian

In this section we describe the FD approximation A_{FD} of the fractional Laplacian on a uniform grid \mathcal{T}_{FD} through its Fourier transform formulation. We also discuss the fast computation of the multiplication of A_{FD} with vectors using FFT. For notational simplicity, we restrict the discussion in two dimensions (2D) in this section. The description of A_{FD} in general d -dimensions is similar.

In terms of the Fourier transform (1.3), the fractional Laplacian reads as

$$(-\Delta)^s u(x, y) = \frac{1}{(2\pi)^2} \int_{-\infty}^{\infty} \int_{-\infty}^{\infty} \widehat{(-\Delta)^s u}(\xi, \eta) e^{ix\xi + iy\eta} d\xi d\eta, \quad (3.1)$$

where

$$\widehat{(-\Delta)^s u}(\xi, \eta) = (\xi^2 + \eta^2)^s \hat{u}(\xi, \eta) \quad (3.2)$$

and \hat{u} is the continuous Fourier transform of u . Consider a 2D uniform grid with spacing h_{FD} ,

$$(x_j, y_k) = (jh_{\text{FD}}, kh_{\text{FD}}), \quad j, k = 0, \pm 1, \pm 2, \dots$$

Applying the discrete Fourier transform to the 5-point central FD approximation of the Laplacian, we obtain the the discrete Fourier transform of an FD approximation of the fractional Laplacian as

$$\widetilde{(-\Delta_h)^s u}(\xi, \eta) = \frac{1}{h_{\text{FD}}^{2s}} \left(4\sin^2\left(\frac{\xi h_{\text{FD}}}{2}\right) + 4\sin^2\left(\frac{\eta h_{\text{FD}}}{2}\right) \right)^s \check{u}(\xi, \eta), \quad (3.3)$$

where $\check{u}(\xi, \eta)$ is the discrete Fourier transform of u on the uniform grid, i.e.,

$$\check{u}(\xi, \eta) = \sum_{m,n} u_{m,n} e^{-ix_m \xi - iy_n \eta}, \quad (\xi, \eta) \in \left(-\frac{\pi}{h_{\text{FD}}}, \frac{\pi}{h_{\text{FD}}}\right) \times \left(-\frac{\pi}{h_{\text{FD}}}, \frac{\pi}{h_{\text{FD}}}\right).$$

Then, the uniform-grid FD approximation of the fractional Laplacian is given by

$$\begin{aligned} (-\Delta_h)^s u(x_j, y_k) &= \frac{h_{\text{FD}}^2}{(2\pi)^2} \int_{-\frac{\pi}{h_{\text{FD}}}}^{\frac{\pi}{h_{\text{FD}}}} \int_{-\frac{\pi}{h_{\text{FD}}}}^{\frac{\pi}{h_{\text{FD}}}} \widetilde{(-\Delta_h)^s u}(\xi, \eta) e^{ix_j \xi + iy_k \eta} d\xi d\eta \\ &= \frac{1}{(2\pi)^2 h_{\text{FD}}^{2s}} \sum_{m=-\infty}^{\infty} \sum_{n=-\infty}^{\infty} u_{m,n} \int_{-\pi}^{\pi} \int_{-\pi}^{\pi} \psi(\xi, \eta) e^{i(j-m)\xi + i(k-n)\eta} d\xi d\eta, \end{aligned}$$

where

$$\psi(\xi, \eta) = \left(4\sin^2\left(\frac{\xi}{2}\right) + 4\sin^2\left(\frac{\eta}{2}\right) \right)^s. \quad (3.4)$$

We can rewrite this into

$$(-\Delta_h)^s u(x_j, y_k) = \frac{1}{h_{\text{FD}}^{2s}} \sum_{m=-\infty}^{\infty} \sum_{n=-\infty}^{\infty} T_{j-m, k-n} u_{m,n}, \quad (3.5)$$

where

$$T_{p,q} = \frac{1}{(2\pi)^2} \int_{-\pi}^{\pi} \int_{-\pi}^{\pi} \psi(\xi, \eta) e^{ip\xi + iq\eta} d\xi d\eta, \quad p, q = 0, \pm 1, \pm 2, \dots \quad (3.6)$$

Obviously, $T_{p,q}$'s are the Fourier coefficients of the function $\psi(\xi, \eta)$. It is not difficult to see

$$T_{-p,-q} = T_{p,q}, \quad T_{-p,q} = T_{p,q}, \quad T_{p,-q} = T_{p,q}. \quad (3.7)$$

Except for one dimension, the matrix T needs to be approximated numerically (cf. Section 5).

For a function u vanishing in Ω^c , (3.5) reduces to a finite double summation as

$$(-\Delta_h)^s u(x_j, y_k) = \frac{1}{h_{\text{FD}}^{2s}} \sum_{m=-N_{\text{FD}}}^{N_{\text{FD}}} \sum_{n=-N_{\text{FD}}}^{N_{\text{FD}}} T_{j-m, k-n} u_{m,n}, \quad -N_{\text{FD}} \leq j, k \leq N_{\text{FD}}. \quad (3.8)$$

From this, we obtain the FD approximation of the fractional Laplacian on the uniform mesh \mathcal{T}_{FD} (after ignoring the factor $1/h_{\text{FD}}^{2s}$) as

$$A_{\text{FD}} = \left(A_{(j,k),(m,n)} = T_{j-m,k-n} \right)_{(2N_{\text{FD}}+1)^2 \times (2N_{\text{FD}}+1)^2}, \quad -N_{\text{FD}} \leq j, k, m, n \leq N_{\text{FD}}. \quad (3.9)$$

This indicates that A_{FD} is a block Toeplitz matrix with Toeplitz blocks. Moreover, it is known [28] that A_{FD} is symmetric and positive definite. For easy reference but without causing confusion, hereafter both matrices A_{FD} and T will be referred to as the stiffness matrix of the uniform-grid FD approximation.

The multiplication of A_{FD} with vectors can be computed efficiently using FFT. Assume that an approximation of T has been obtained. We first compute the discrete Fourier transform of T . Notice that the entries of T involved in (3.8) are: $T_{m,n}$, $-2N_{\text{FD}} \leq m, n \leq 2N_{\text{FD}}$. Thus, the discrete Fourier transform of T is given by

$$\check{T}_{p,q} = \sum_{m=-2N_{\text{FD}}}^{2N_{\text{FD}}-1} \sum_{n=-2N_{\text{FD}}}^{2N_{\text{FD}}-1} T_{m,n} e^{-\frac{i2\pi(m+2N_{\text{FD}})(p+2N_{\text{FD}})}{4N_{\text{FD}}} - \frac{i2\pi(n+2N_{\text{FD}})(q+2N_{\text{FD}})}{4N_{\text{FD}}}}, \quad -2N_{\text{FD}} \leq p, q \leq 2N_{\text{FD}}. \quad (3.10)$$

Here, $2N_{\text{FD}}$ has been added to the indices m , n , p , and q so that the corresponding indices have the range from 0 to $4N_{\text{FD}}-1$. As a result, Matlab's function **fft.m** can be used for computing (3.10) directly. Then, $T_{m,n}$'s can be expressed using the inverse discrete Fourier transform as

$$T_{m,n} = \frac{1}{(4N_{\text{FD}})^2} \sum_{p=-2N_{\text{FD}}}^{2N_{\text{FD}}-1} \sum_{q=-2N_{\text{FD}}}^{2N_{\text{FD}}-1} \check{T}_{p,q} e^{\frac{i2\pi(m+2N_{\text{FD}})(p+2N_{\text{FD}})}{4N_{\text{FD}}} + \frac{i2\pi(n+2N_{\text{FD}})(q+2N_{\text{FD}})}{4N_{\text{FD}}}}.$$

From this, we have

$$\begin{aligned} (A_{\text{FD}} \vec{u}_{\text{FD}})_{(j,k)} &= \sum_{m=-N_{\text{FD}}}^{N_{\text{FD}}} \sum_{n=-N_{\text{FD}}}^{N_{\text{FD}}} T_{j-m,k-n} u_{m,n} \\ &= \frac{1}{(4N_{\text{FD}})^2} \sum_{p=-2N_{\text{FD}}}^{2N_{\text{FD}}-1} \sum_{q=-2N_{\text{FD}}}^{2N_{\text{FD}}-1} \check{T}_{p,q} \sum_{m=-N_{\text{FD}}}^{N_{\text{FD}}} \sum_{n=-N_{\text{FD}}}^{N_{\text{FD}}} u_{m,n} \\ &\quad \cdot e^{\frac{i2\pi(j-m+2N_{\text{FD}})(p+2N_{\text{FD}})}{4N_{\text{FD}}} + \frac{i2\pi(k-n+2N_{\text{FD}})(q+2N_{\text{FD}})}{4N_{\text{FD}}}}. \end{aligned}$$

This can be rewritten as

$$\begin{aligned} (A_{\text{FD}} \vec{u}_{\text{FD}})_{(j,k)} &= \frac{1}{(4N_{\text{FD}})^2} \sum_{p=-2N_{\text{FD}}}^{2N_{\text{FD}}-1} \sum_{q=-2N_{\text{FD}}}^{2N_{\text{FD}}-1} \check{T}_{p,q} \check{u}_{p,q} (-1)^{p+2N_{\text{FD}}+q+2N_{\text{FD}}} \\ &\quad \cdot e^{\frac{i2\pi(p+2N_{\text{FD}})(j+2N_{\text{FD}})}{4N_{\text{FD}}} + \frac{i2\pi(q+2N_{\text{FD}})(k+2N_{\text{FD}})}{4N_{\text{FD}}}}, \quad (3.11) \end{aligned}$$

where

$$\begin{aligned} \check{u}_{p,q} &= \sum_{m=-2N_{\text{FD}}-1}^{2N_{\text{FD}}-1} \sum_{n=-2N_{\text{FD}}}^{2N_{\text{FD}}-1} \tilde{u}_{m,n} e^{-\frac{i2\pi(m+2N_{\text{FD}})(p+2N_{\text{FD}})}{4N_{\text{FD}}}} - \frac{i2\pi(n+2N_{\text{FD}})(q+2N_{\text{FD}})}{4N_{\text{FD}}}, \\ \tilde{u}_{m,n} &= \begin{cases} u_{m,n}, & \text{for } -N_{\text{FD}} \leq m, n \leq N_{\text{FD}}, \\ 0, & \text{otherwise.} \end{cases} \end{aligned} \quad (3.12)$$

Notice that that (3.10), (3.11), and (3.12) can be computed using FFT. Since the cost of FFT is $\mathcal{O}(N_{\text{FD}}^d \log(N_{\text{FD}}^d))$ flops (in d -dimensions), the number of the flops needed to carry out the multiplication of A_{FD} with a vector is

$$\mathcal{O}(N_{\text{FD}}^d \log(N_{\text{FD}}^d)), \quad (3.13)$$

which is almost linearly proportional to the number of nodes of the uniform grid \mathcal{T}_{FD} . Comparatively, the direction computation of the multiplication of A_{FD} with a vector without using FFT requires $\mathcal{O}(N_{\text{FD}}^{2d})$ flops.

4 Importance of approximating the stiffness matrix T accurately

The accuracy in approximating T can have a significant impact on the accuracy of computing $A_{\text{FD}}\vec{u}_{\text{FD}}$ (and then the accuracy in the numerical solution of BVP (1.1)) due to the fact that A_{FD} is a dense matrix. To explain this, let us assume the error in approximating T is $10^{-\delta}$, where δ is a positive integer. Then the error in computing $A_{\text{FD}}\vec{u}_{\text{FD}}$ (cf. (3.8)) is bounded (in d -dimensions) by

$$\frac{1}{R_{\text{FD}}^{2s}} (2N_{\text{FD}}+1)^d N_{\text{FD}}^{2s} \times 10^{-\delta} \|u\|_{L^\infty(\Omega)}. \quad (4.1)$$

For fixed R_{FD} , δ , and $\|u\|_{L^\infty(\Omega)}$, this bound goes to infinity as $N_{\text{FD}} \rightarrow \infty$. This implies that the error in computing $A_{\text{FD}}\vec{u}_{\text{FD}}$ and therefore, the error in the whole computation of BVP (1.1), will be dominated by the error in approximating T at some point as the mesh is refined and increase after that point if the mesh is further refined.

To see this more clearly, we take $R_{\text{FD}} = 1$ and $\|u\|_{L^\infty(\Omega)} = 1$ and assume that the discretization error for BVP (1.1) is $\mathcal{O}(1/N_{\text{FD}})$ (first-order) or $\mathcal{O}(1/N_{\text{FD}}^2)$ (second-order). The bound in (4.1) is plotted as a function of N_{FD} in Fig. 1 against $1/N_{\text{FD}}$ and $1/N_{\text{FD}}^2$ for two levels of the accuracy in approximating T (10^{-9} and 10^{-12}) and in 2D and 3D. From the figure we can see that there exists an equilibrium point (N_{FD}^e, E^e) where the bound (4.1) and the discretization error intersect. For example, in Fig. 1(b) we have $(N_{\text{FD}}^e, E^e) \approx (700, 1.5 \times 10^{-3})$ and $(200, 3 \times 10^{-5})$ for the first-order and second-order discretization error, respectively. Generally speaking, for $N_{\text{FD}} \leq N_{\text{FD}}^e$, the overall error is dominated by the discretization error (regardless of the order) and decreases as N_{FD} increases. For

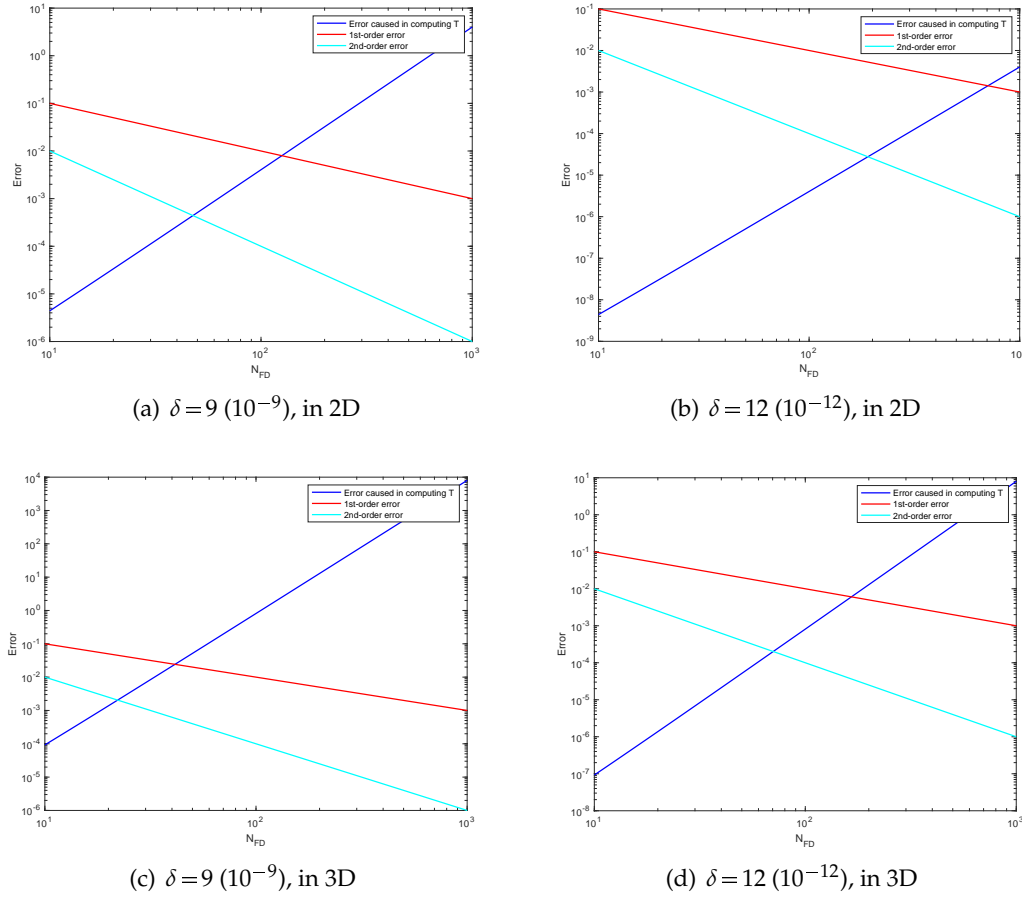


Figure 1: The error in computing T is plotted as a function of N_{FD} against the discretization error.

$N_{FD} \geq N_{FD}^e$, on the other hand, the overall error is dominated by the error in approximating T and increases with N_{FD} . Thus, for a fixed level of accuracy in approximating T , **the total error in the computed solution is expected to decrease for small N_{FD} but then increase as N_{FD} increases**. The turning of the error behavior occurs at larger N_{FD} and larger E^e for the first order discretization error than the second-order one. Moreover, N_{FD}^e becomes larger and E^e becomes smaller when T is approximated more accurately. Finally, the figure shows that N_{FD}^e is smaller for 3D than for 2D for the same level of accuracy in approximating T . For example, in Fig. 1(d) $N_{FD}^e \approx 180$ and 70 for the first-order and second-order discretization error, respectively. These are compared with $N_{FD}^e \approx 700$ and 200 for 2D in Fig. 1(b).

To further demonstrate the effect, we consider Example (1.4) with GoFD with the FFT approximation of the stiffness matrix T (cf. Section 5.1). The accuracy in approximating T in this approach is determined by the number of nodes used in each axial direction,

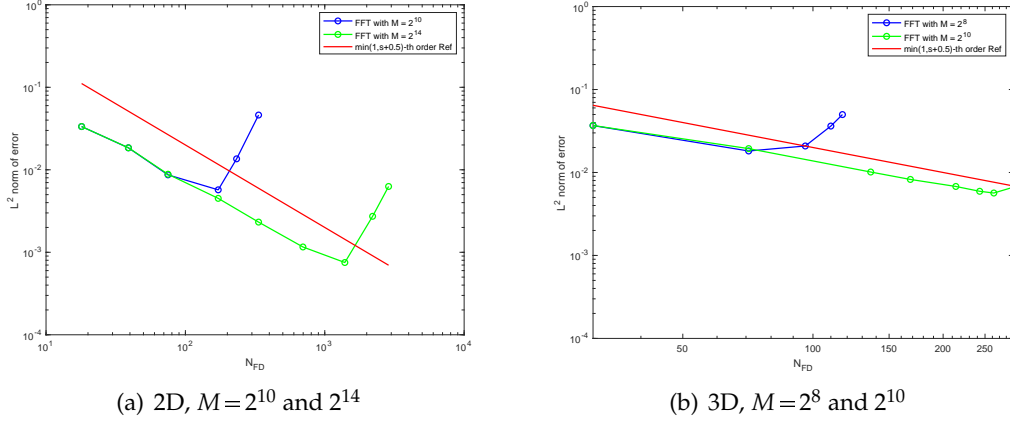


Figure 2: Example (1.4) with $s=0.5$. Convergence histories of GoFD with the stiffness matrix T being computed with FFT with various levels of accuracy (through different values of M).

M . The solution error in L^2 norm is plotted as a function of N_{FD} for a fixed M in Fig. 2 for 2D and 3D. Quasi-uniform meshes are used for Ω for the computation. It is known numerically that the error of GoFD converges at the rate $\mathcal{O}(h^{\min(1, s+0.5)})$ for quasi-uniform meshes. We can see that for small N_{FD} , the error decrease at this expected rate. But after a certain N_{FD} , the error begins to increase. The turning of the error behavior occurs at a larger N_{FD} for a larger M (corresponding to a higher level of accuracy in approximating T). These results confirm the analysis made earlier in this section.

It should be pointed out that the effect of the error in approximating the stiffness matrix on the overall computational accuracy is not unique to the FD/GoFD approximation discussed in this work. It can also happen with finite element and other FD approximations of the fractional Laplacian where the stiffness matrix is dense and needs to be approximated numerically.

5 Approximation of the stiffness matrix T

In this section we describe four approaches to approximate the stiffness matrix T . Recall that T is given in (3.6) in 2D. Its d -dimensional form is

$$T_{\vec{p}} = \frac{1}{(2\pi)^d} \iint_{(-\pi, \pi)^d} \psi(\vec{\xi}) e^{i\vec{p} \cdot \vec{\xi}} d\vec{\xi}, \quad 0 \leq \vec{p} \leq 2N_{FD}, \quad (5.1)$$

where

$$\psi = \psi(\vec{\xi}) \equiv \left(4 \sum_{j=1}^d \sin^2 \left(\frac{\xi_j}{2} \right) \right)^s. \quad (5.2)$$

In 1D, T has the analytical form (see, e.g., [35]),

$$T_p = \frac{(-1)^p \Gamma(2s+1)}{\Gamma(p+s+1)\Gamma(s-p+1)}, \quad p=0, \dots, 2N_{\text{FD}}. \quad (5.3)$$

In multi-dimensions, T needs to be approximated numerically.

It is useful to recall some properties of the matrix T . Obviously, $T_{\vec{p}}$'s are the Fourier coefficients of the function $\psi = \psi(\vec{\xi})$. Moreover, T needs to be approximated only for $0 \leq \vec{p} \leq 2N_{\text{FD}}$ (or in 2D, $0 \leq p, q \leq 2N_{\text{FD}}$) due to the symmetry (3.7). Furthermore, $T_{\vec{p}}$ has the asymptotic decay

$$T_{\vec{p}} = \mathcal{O}\left(\frac{1}{|\vec{p}|^{d+2s}}\right), \quad \text{as } |\vec{p}| \rightarrow \infty. \quad (5.4)$$

This is known analytically in 1D [35]. In multi-dimensions, such analytical results are not available. Numerical verifications for $d=1, 2$, and 3 can be seen in Fig. 3. From (3.9), we can see that the asymptotic decay of $T_{\vec{p}}$ for large $|\vec{p}|$ represents the decay of the entries of A_{FD} away from the diagonal line. Such asymptotic estimates are needed for the domain truncation and error estimation in the numerical solution of inhomogeneous Dirichlet problems of the fractional Laplacian [29].

5.1 The FFT approach

We describe this approach in 2D. For any given integer $M \geq 2N_{\text{FD}} + 1$, define a uniform grid for $(-\pi, \pi) \times (-\pi, \pi)$ as

$$(\xi_j, \eta_k) = \pi\left(\frac{2j}{M} - 1, \frac{2k}{M} - 1\right), \quad j, k = 0, 1, \dots, M. \quad (5.5)$$

Then, using the composite trapezoidal rule we have

$$\begin{aligned} T_{p,q} &= \frac{1}{(2\pi)^2} \sum_{j=0}^{M-1} \sum_{k=0}^{M-1} \int_{\xi_j}^{\xi_{j+1}} \int_{\eta_k}^{\eta_{k+1}} \psi(\xi, \eta) \cdot e^{ip\xi + iq\eta} d\xi d\eta \\ &\approx \frac{(-1)^{p+q}}{M^2} \sum_{j=0}^{M-1} \sum_{k=0}^{M-1} \psi(\xi_j, \eta_k) \cdot e^{\frac{ipj2\pi}{M} + \frac{iqk2\pi}{M}}, \quad 0 \leq p, q \leq 2N_{\text{FD}}, \end{aligned} \quad (5.6)$$

which can be computed with FFT. The number of flops required for this (in d -dimensions) is

$$\mathcal{O}(M^d \log(M^d)), \quad (5.7)$$

where $M \geq 2N_{\text{FD}} + 1$.

To see how accurate this approach is, we apply it to the 1D case and compare the obtained approximation with the analytical expression (5.3). The error is listed in Table 1

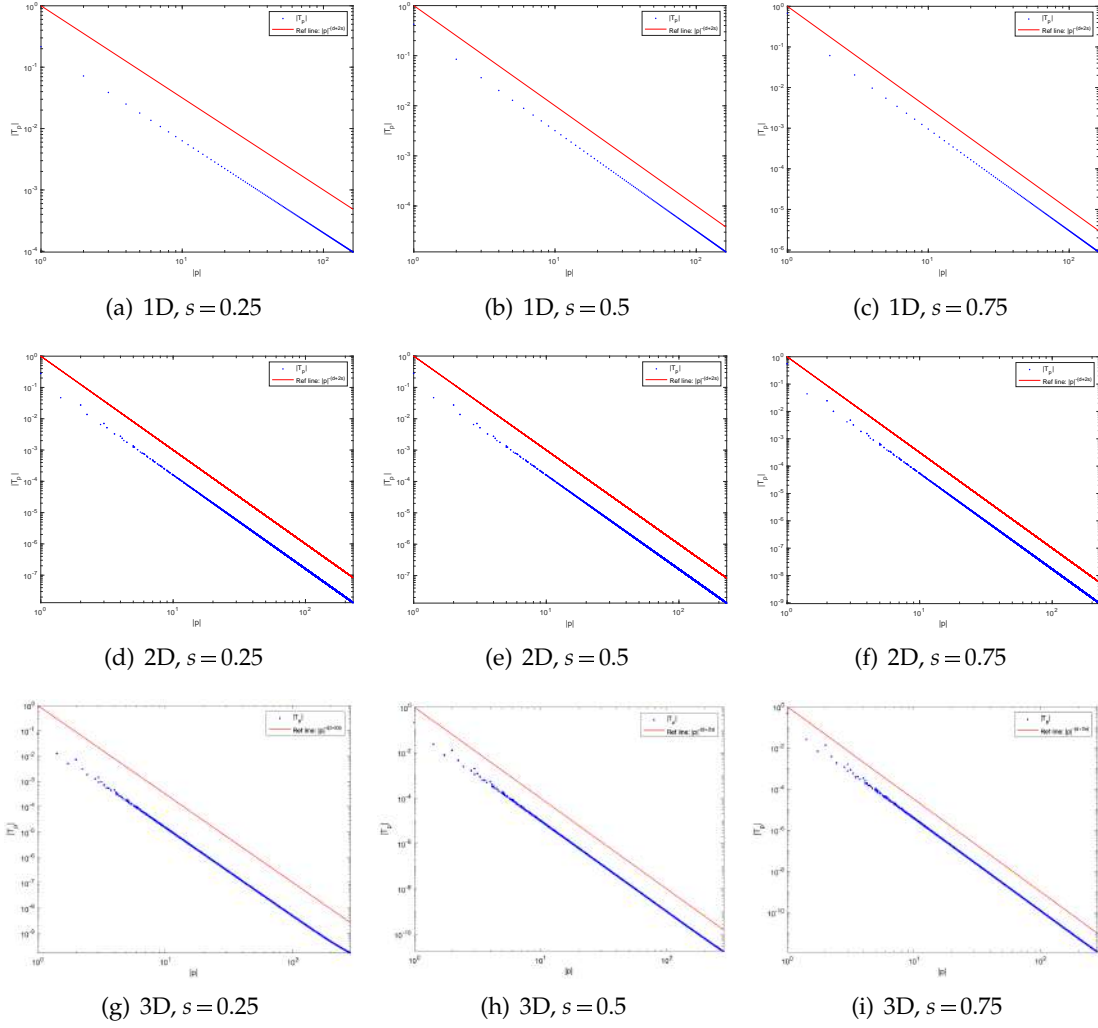


Figure 3: The decay of $T_{\vec{p}}$ as $|\vec{p}| \rightarrow \infty$ for $s=0.25, 0.50$, and 0.75 . The reference line is $T_{\vec{p}} = |\vec{p}|^{-(d+2s)}$.

for $M = 2^{10}$ and 2^{14} . It can be seen that this FFT approach performs much more accurate for large s than small ones. The difficulty with small s comes from the fact that $\psi(\vec{\xi})$ has a cusp at the origin.

Filon's [23] approach for highly oscillatory integrals and Richardson's extrapolation have been considered for approximating T in [28]. Some other numerical integral schemes, such as composite Simpson's and Boole's rules, can also be used (to improve convergence order for smooth integrants). Unfortunately, their convergence behavior for small s is not much different from those with the composite trapezoidal rule used here due to the low regularity of the function $\psi(\vec{\xi})$ at the origin for small s .

Table 1: The error in approximating T in one dimension using the FFT, non-uniform FFT, and modified spectral approaches. The error is calculated as the maximum norm of the difference between the approximation and analytical expression (5.3). $N_{\text{FD}} = 81$ is used.

Approximation	M	s				
		0.1	0.25	0.5	0.75	0.9
FFT	2^{10}	2.477e-04	3.247e-05	1.050e-06	2.609e-08	1.713e-09
	2^{14}	8.812e-06	4.970e-07	3.902e-09	2.337e-11	6.516e-13
nuFFT	2^{10}	1.486e-06	1.798e-06	2.543e-06	3.597e-06	4.428e-06
	2^{14}	5.735e-09	7.024e-09	9.934e-09	1.4055e-08	1.730e-08
Modified Spectral	2^{10}	7.550e-07	2.962e-07	1.050e-06	2.792e-06	4.723e-06
	2^{14}	7.387e-08	2.457e-09	3.902e-09	1.037e-08	1.755e-08

5.2 The non-uniform FFT approach

A strategy to deal with the low regularity of $\psi(\vec{\xi})$ at the origin is to use non-uniform sampling points. For example, we use

$$(\xi_j, \eta_k) = \pi \left(\left(\frac{2j}{M} - 1 \right)^2 \text{sign} \left(\frac{2j}{M} - 1 \right), \left(\frac{2k}{M} - 1 \right)^2 \text{sign} \left(\frac{2k}{M} - 1 \right) \right), \quad j, k = 0, 1, \dots, M, \quad (5.8)$$

which clusters at the origin. Then, we apply the composite trapezoidal rule and obtain

$$T_{p,q} \approx \frac{1}{(2\pi)^2} \sum_{j=0}^{M-1} \sum_{k=0}^{M-1} \frac{(\xi_{j+1} - \xi_{j-1})(\eta_{k+1} - \eta_{k-1})}{4} \psi(\xi_j, \eta_k) \cdot e^{ip\xi_j + iq\eta_k}, \quad 0 \leq p, q \leq 2N_{\text{FD}}, \quad (5.9)$$

which can be computed using the non-uniform FFT [8,9,20]. In our computation, we use **finufft** developed by Barnett et al. [8,9]. Matlab's function **nufft.m** can also be used for this purpose but is slower than **finufft**.

This approach is applied to the 1D case and the error is listed in Table 1. It can be seen that this approach improves the accuracy significantly for small s than the FFT approach although it is inferior to the latter for large s . Moreover, the accuracy of this nuFFT approximation is almost the same for all s in $(0,1)$.

The CPU time is reported in Table 2. It can be seen that, unfortunately, the non-uniform FFT approximation is much more expensive than the FFT approximation. This is especially true for large M or for 3D.

5.3 A spectral approximation

This approach is the spectral approximation of Zhou and Zhang [47] for the fractional Laplacian. It can be interpreted as replacing the integrand and the domain in (5.1) by

Table 2: CPU times (in seconds) taken to compute the matrix T in 2D and 3D for various values of M . $N_{\text{FD}}=81$ and $s=0.5$ are used except for the case with 3D and $M=2^8$ where $N_{\text{FD}}=71$ is used. For the modified spectral approximation, $n_G=64$ is used. The computation was performed on a Macbook Pro with M1 Max and 32 GB memory.

Approximation	2D			3D		
	$M=2^{10}$	$M=2^{12}$	$M=2^{14}$	$M=2^8$	$M=2^9$	$M=2^{10}$
FFT	0.033	0.082	3.879	0.103	1.895	38.09
nuFFT	0.0738	0.503	8.602	6.369	49.94	419.24
Modified Spectral	0.144	0.344	4.519	1.406	4.241	67.21

spherically symmetric ones, i.e.,

$$\psi(\vec{\xi}) = \left(4 \sum_{j=1}^d \sin^2 \left(\frac{\xi_j}{2} \right) \right)^s \implies |\vec{\xi}|^{2s}, \quad (-\pi, \pi)^d \implies B_R(0),$$

where $|\vec{\xi}|^{2s}$ has the same behavior as $\psi(\vec{\xi})$ near the origin and R is chosen such that the ball $B_R(0)$ has the same volume as the cube $(-\pi, \pi)^d$, i.e.,

$$R = 2\sqrt{\pi} \left(\Gamma \left(\frac{d}{2} + 1 \right) \right)^{\frac{1}{d}}. \quad (5.10)$$

Then, we obtain

$$\tilde{T}_{\vec{p}} = \frac{1}{(2\pi)^d} \iint_{B_R(0)} |\vec{\xi}|^{2s} e^{i\vec{p} \cdot \vec{\xi}} d\vec{\xi}. \quad (5.11)$$

The difference between (5.1) and (5.11) is

$$T_{\vec{p}} - \tilde{T}_{\vec{p}} = \frac{1}{(2\pi)^d} \iint_{(-\pi, \pi)^d} \left(\psi(\vec{\xi}) - |\vec{\xi}|^{2s} \right) e^{i\vec{p} \cdot \vec{\xi}} d\vec{\xi} + \frac{1}{(2\pi)^d} \left(\iint_{(-\pi, \pi)^d \setminus B_R(0)} - \iint_{B_R(0) \setminus (-\pi, \pi)^d} \right) |\vec{\xi}|^{2s} e^{i\vec{p} \cdot \vec{\xi}} d\vec{\xi}.$$

The first and second terms on the right-hand side correspond to the differences caused by replacing the integrand and integration domain, respectively. Using the formula of the Fourier transform of radial functions, we can rewrite (5.11) into

$$\tilde{T}_{\vec{p}} = \frac{1}{(2\pi)^{\frac{d}{2}} |\vec{p}|^{\frac{d}{2}-1}} \int_0^R r^{2s+\frac{d}{2}} J_{\frac{d}{2}-1}(|\vec{p}|r) dr, \quad (5.12)$$

where $J_{\frac{d}{2}-1}(\cdot)$ is a Bessel function. From Prudnikov et al. [38, 2.12.4 (3)] (with $\beta=1$), we can rewrite this into

$$\tilde{T}_{\vec{p}} = \frac{R^{d+2s}}{(2\pi)^{\frac{d}{2}} 2^{\frac{d}{2}} (s+\frac{d}{2}) \Gamma(\frac{d}{2})} {}_1F_2 \left(2s + \frac{d}{2}; 2s + \frac{d}{2} + 1, \frac{d}{2}; -\frac{R^2 |\vec{p}|^2}{4} \right), \quad (5.13)$$

where ${}_1F_2(\cdot)$ is a hypergeometric function [5]. Hypergeometric functions are supported in many packages, including Matlab (**hypergeom.m**). However, it can be extremely slow to compute $\tilde{T}_{\vec{p}}$ through (5.13) using hypergeometric functions especially when N_{FD} is large.

Here, we propose a new and fast way to compute $\tilde{T}_{\vec{p}}$. When $\vec{p} = \vec{0}$, from (5.11) we have

$$\tilde{T}_{\vec{0}} = \frac{1}{(2\pi)^d} \iint_{B_R(0)} |\vec{\zeta}|^{2s} d\vec{\zeta} = \frac{1}{(2\pi)^d} \int_0^R d\pi \frac{\pi^{\frac{d}{2}-1+2s}}{\Gamma(\frac{d}{2}+1)} dr = \frac{2R^{d+2s}}{(d+2s)2^d \pi^{\frac{d}{2}} \Gamma(\frac{d}{2})}. \quad (5.14)$$

When $\vec{p} \neq \vec{0}$, by changing the integral variable in (5.12) we get

$$\tilde{T}_{\vec{p}} = \frac{1}{(2\pi)^{\frac{d}{2}} |\vec{p}|^{2s+d}} \int_0^{R|\vec{p}|} r^{2s+\frac{d}{2}} J_{\frac{d}{2}-1}(r) dr. \quad (5.15)$$

Recall that we need to compute $\tilde{T}_{\vec{p}}$ for $\vec{p} = p$ in 1D for $0 \leq p \leq N_{\text{FD}}$, $\vec{p} = (p, q)$ for $0 \leq p, q \leq N_{\text{FD}}$ in 2D, and $\vec{p} = (p, q, r)$ for $0 \leq p, q, r \leq N_{\text{FD}}$ in 3D. Let $n = (N_{\text{FD}} + 1)^d$. These points are sorted (and renamed if necessary) as

$$|\vec{p}_0| \leq |\vec{p}_1| \leq \dots \leq |\vec{p}_n|.$$

In actual computation, we can remove repeated points to save time. Then, we apply a Gaussian quadrature (of n_G points) to the integrals

$$\int_{R|\vec{p}_{j-1}|}^{R|\vec{p}_j|} r^{2s+\frac{d}{2}} J_{\frac{d}{2}-1}(r) dr, \quad j = 1, \dots, n.$$

Finally, we obtain

$$\tilde{T}_{\vec{p}_k} = \frac{1}{(2\pi)^{\frac{d}{2}} |\vec{p}_k|^{2s+d}} \sum_{j=1}^k \int_{R|\vec{p}_{j-1}|}^{R|\vec{p}_j|} r^{2s+\frac{d}{2}} J_{\frac{d}{2}-1}(r) dr, \quad k = 1, \dots, n. \quad (5.16)$$

The total number of flops required to compute \tilde{T} is

$$\mathcal{O}(n_G (N_{\text{FD}} + 1)^d), \quad (5.17)$$

which is linearly proportional to the total number of nodes of the uniform grid \mathcal{T}_{FD} . This cost is smaller than or comparable with that of the FFT approach, (5.7). Since the cost of computing this spectral approximation is independent of M , we do not list the CPU time for this approach in Table 2. Nevertheless, we can get an idea from the CPU time for the modified spectral approach (cf. Section 5.4) which employs the current approach for computing one of its integrals.

It has been shown in [47] that the stiffness matrix (5.11) can lead to accurate approximations to BVP (1.1) (also cf. Section 7). It is worth emphasizing that (5.11) is different from (and not close to) the stiffness matrix (5.1). In the following, we show that (5.11) has asymptotic rates different from (5.4) for the stiffness matrix (5.1).

Proposition 5.1. The stiffness matrix \tilde{T} defined in (5.11) has the decay

$$\tilde{T}_{\vec{p}} = \mathcal{O}\left(\frac{1}{|\vec{p}|^{\frac{d+1}{2}}}\right), \quad \text{as } |\vec{p}| \rightarrow \infty. \quad (5.18)$$

Proof. It is known that the Bessel function $J_{\frac{d}{2}-1}$ can be expressed as

$$J_{\frac{d}{2}-1}(r) = \sqrt{\frac{2}{\pi r}} \cos\left(r - \frac{(d-1)\pi}{4}\right) + \mathcal{O}(r^{-\frac{3}{2}}).$$

Thus, as $|\vec{p}| \rightarrow \infty$ we have

$$\begin{aligned} & \int_0^{R|\vec{p}|} r^{2s+\frac{d}{2}} J_{\frac{d}{2}-1}(r) dr \\ &= \int_0^1 r^{2s+\frac{d}{2}} J_{\frac{d}{2}-1}(r) dr + \sqrt{\frac{2}{\pi}} \int_1^{R|\vec{p}|} r^{2s+\frac{d-1}{2}} \left[\cos\left(r - \frac{(d-1)\pi}{4}\right) + \mathcal{O}(r^{-1}) \right] dr \\ &= \int_0^1 r^{2s+\frac{d}{2}} J_{\frac{d}{2}-1}(r) dr + \sqrt{\frac{2}{\pi}} \int_1^{R|\vec{p}|} r^{2s+\frac{d-1}{2}} \cos\left(r - \frac{(d-1)\pi}{4}\right) dr + \mathcal{O}(|\vec{p}|^{2s+\frac{d-1}{2}}) \\ &= \int_0^1 r^{2s+\frac{d}{2}} J_{\frac{d}{2}-1}(r) dr + \mathcal{O}(|\vec{p}|^{2s+\frac{d-1}{2}}) + \sqrt{\frac{2}{\pi}} r^{2s+\frac{d-1}{2}} \sin\left(r - \frac{(d-1)\pi}{4}\right) \Big|_1^{R|\vec{p}|} \\ &\quad - \left(2s + \frac{d-1}{2}\right) \sqrt{\frac{2}{\pi}} \int_1^{R|\vec{p}|} r^{2s+\frac{d-3}{2}} \sin\left(r - \frac{(d-1)\pi}{4}\right) dr \\ &= \int_0^1 r^{2s+\frac{d}{2}} J_{\frac{d}{2}-1}(r) dr + \mathcal{O}(|\vec{p}|^{2s+\frac{d-1}{2}}) + \mathcal{O}(|\vec{p}|^{2s+\frac{d-1}{2}}) + \mathcal{O}(|\vec{p}|^{2s+\frac{d-1}{2}}) \\ &= \mathcal{O}(|\vec{p}|^{2s+\frac{d-1}{2}}). \end{aligned}$$

The asymptotic (5.18) follows this and (5.15). □

Proposition 5.2. In 1D, the stiffness matrix \tilde{T} defined in (5.11) has the decay

$$\tilde{T}_p = \mathcal{O}\left(\frac{1}{|p|^{1+\min(1,2s)}}\right), \quad \text{as } |p| \rightarrow \infty. \quad (5.19)$$

Proof. From (5.11), we have

$$\tilde{T}_p = \frac{1}{2\pi} \int_{-\pi}^{\pi} |\xi|^{2s} e^{ip\xi} d\xi = \frac{1}{\pi} \int_0^{\pi} \xi^{2s} \cos(p\xi) d\xi = \pi^{2s} \int_0^1 \xi^{2s} \cos(p\xi\pi) d\xi.$$

From Gradshteyn and Ryzhik [24, Page 436, 3.761 (6)], we have

$$\tilde{T}_p = \frac{\pi^{2s}}{2(1+2s)} (M(1+2s, 2+2s, ip\pi) + M(1+2s, 2+2s, -ip\pi)),$$

where $M(a, b, z)$ is the Kummer's confluent hypergeometric function.

As $p \rightarrow \infty$, the Kummer's function has the asymptotic

$$\begin{aligned} & M(1+2s, 2+2s, ip\pi) \\ &= \frac{e^{ip\pi}(ip\pi)^{-1}}{\Gamma(1+2s)} \left[1 + \frac{(-2s)(1)}{1!}(ip\pi)^{-1} + \mathcal{O}(p^{-2}) \right] + \frac{e^{\pi i(1+2s)}(ip\pi)^{-(1+2s)}}{\Gamma(1)} \left[1 + \mathcal{O}(p^{-1}) \right] \\ &= \frac{e^{ip\pi}(ip\pi)^{-1}}{\Gamma(1+2s)} + \frac{2se^{ip\pi}}{(p\pi)^2\Gamma(1+2s)} + \frac{e^{\pi i(1+2s)}(ip\pi)^{-(1+2s)}}{\Gamma(1)} + \mathcal{O}(p^{-(2+2s)}). \end{aligned}$$

Noticing $i = e^{i\pi/2}$, we get

$$M(1+2s, 2+2s, ip\pi) \sim \frac{e^{i(p\pi - \frac{\pi}{2})}}{p\pi\Gamma(1+2s)} + \frac{2se^{ip\pi}}{(p\pi)^2\Gamma(1+2s)} + \frac{e^{i(1+2s)\frac{\pi}{2}}}{(p\pi)^{1+2s}} + \mathcal{O}(p^{-(2+2s)})$$

and

$$\begin{aligned} & M(1+2s, 2+2s, ip\pi) + M(1+2s, 2+2s, -ip\pi) \\ &= \frac{2\cos(x\pi - \frac{\pi}{2})}{p\pi\Gamma(1+2s)} + \frac{4s\cos(p\pi)}{(p\pi)^2\Gamma(1+2s)} + \frac{2\cos((1+2s)\pi/2)}{(p\pi)^{1+2s}} + \mathcal{O}(p^{-(2+2s)}). \end{aligned}$$

Combining the above results, we get

$$\tilde{T}_p = \frac{\pi^{2s}}{2(1+2s)} \left[\frac{2\sin(p\pi)}{p\pi\Gamma(1+2s)} + \frac{4s\cos(p\pi)}{(p\pi)^2\Gamma(1+2s)} + \frac{2\cos((1+2s)\pi/2)}{(p\pi)^{1+2s}} \right] + \mathcal{O}(p^{-(2+2s)}). \quad (5.20)$$

Recall that p is a positive integer and $\sin(p\pi) = 0$. Thus,

$$\begin{aligned} \tilde{T}_p &= \frac{\pi^{2s}}{2(1+2s)} \left[\frac{4s\cos(p\pi)}{(p\pi)^2\Gamma(1+2s)} + \frac{2\cos((1+2s)\pi/2)}{(p\pi)^{1+2s}} \right] + \mathcal{O}(p^{-(2+2s)}) \\ &= \mathcal{O}(p^{-2}) + \mathcal{O}(p^{-(1+2s)}) = \mathcal{O}(p^{-(1+\min(1, 2s))}). \end{aligned}$$

This completes the proof. \square

Numerical results in Fig. 4 verify the decay rates of $\tilde{T}_{\vec{p}}$ as in Propositions 5.1 and 5.2. Moreover, Fig. 4 shows different patterns of the distribution of \tilde{T} than those in Fig. 3 for the stiffness matrix T . Specifically, the entries of T stay closely along the decay line whereas the entries of \tilde{T} spread out more below the decay line.

5.4 A modified spectral approximation

This approximation is a modification of the spectral approximation discussed in the previous subsection. We rewrite (5.1) into

$$T_{\vec{p}} = \frac{1}{(2\pi)^d} \iint_{(-\pi, \pi)^d} \left(\psi(\vec{\xi}) - |\vec{\xi}|^{2s} \right) e^{i\vec{p} \cdot \vec{\xi}} d\vec{\xi} + \frac{1}{(2\pi)^d} \iint_{(-\pi, \pi)^d} |\vec{\xi}|^{2s} e^{i\vec{p} \cdot \vec{\xi}} d\vec{\xi}. \quad (5.21)$$

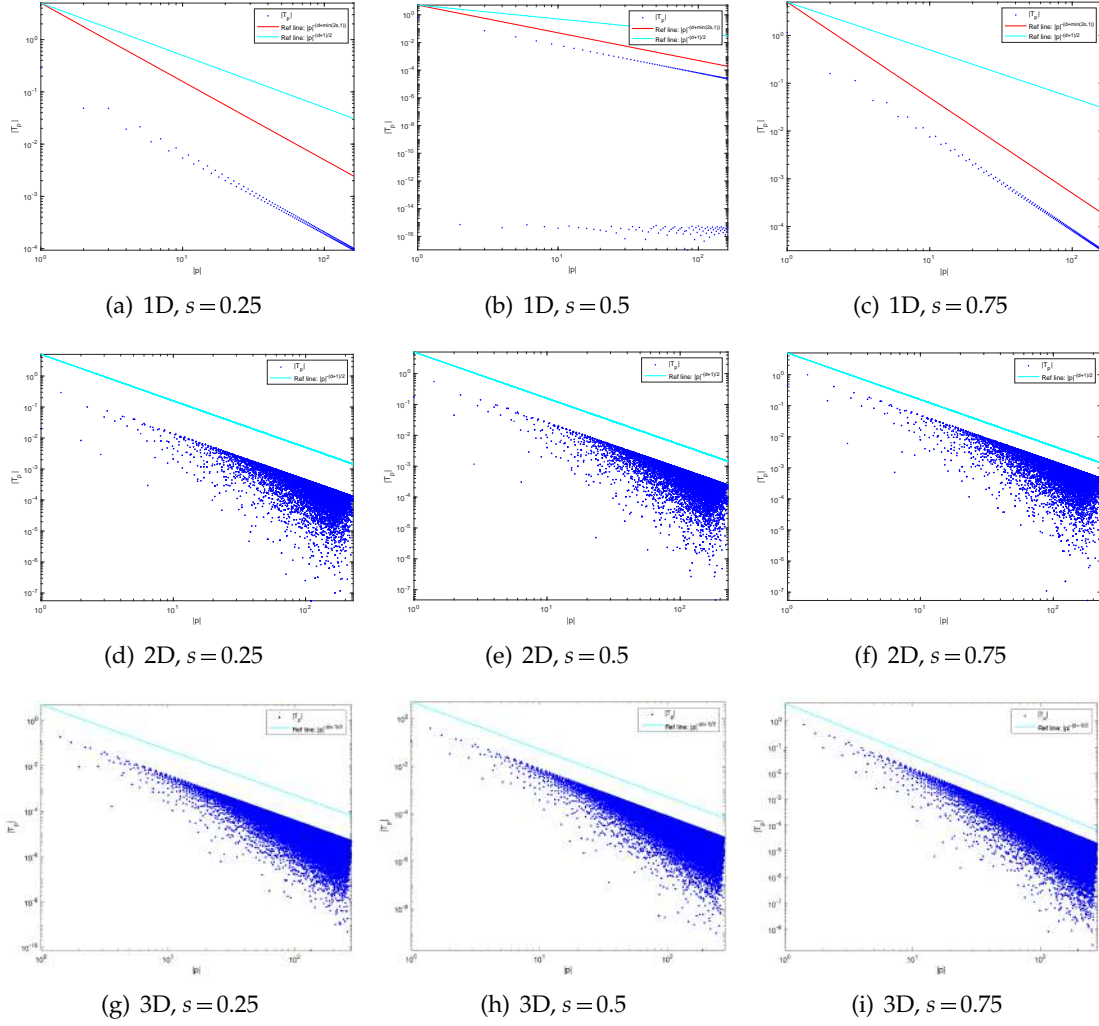


Figure 4: The decay of $\tilde{T}_{\vec{p}}$ as $|\vec{p}| \rightarrow \infty$ for $s=0.25, 0.50$, and 0.75 . The reference lines are $T_{\vec{p}} = |\vec{p}|^{-(d+2s)}$ (for 1D) and $T_{\vec{p}} = |\vec{p}|^{-(d+1)/2}$ (for 2D and 3D).

We expect that the low regularity issue can be avoided in the first integral on the right-hand side since $\psi(\vec{\zeta})$ and $|\vec{\zeta}|^{2s}$ have similar behavior near the origin. Moreover, we would like to use the algorithm (for spherically symmetric integrals) in the previous subsection for the second integral. Thus, we approximate the second integral by replacing the cube by a ball with the radius given in (5.10). We get

$$\tilde{T}_{\vec{p}} = \frac{1}{(2\pi)^d} \iint_{(-\pi, \pi)^d} \left(\psi(\vec{\zeta}) - |\vec{\zeta}|^{2s} \right) e^{i\vec{p} \cdot \vec{\zeta}} d\vec{\zeta} + \frac{1}{(2\pi)^d} \iint_{B_R(0)} |\vec{\zeta}|^{2s} e^{i\vec{p} \cdot \vec{\zeta}} d\vec{\zeta}. \quad (5.22)$$

Notice that the second term on the right-hand side of the above equation is actually the spectral approximation (5.11) discussed in the previous subsection. Thus, the current and previous approximations differ in the first term. We apply the FFT approach of Section 5.1 to the first integral and the spectral approach of Section 5.3 to the second integral on the right-hand side. The cost of the current approach is essentially the addition of those for the FFT and spectral approaches. The difference between (5.1) and (5.22) is

$$T_{\vec{p}} - \tilde{T}_{\vec{p}} = \frac{1}{(2\pi)^d} \left(\iint_{(-\pi, \pi)^d \setminus B_R(0)} - \iint_{B_R(0) \setminus (-\pi, \pi)^d} \right) |\vec{\xi}|^{2s} e^{i\vec{p} \cdot \vec{\xi}} d\vec{\xi}. \quad (5.23)$$

In 1D, $B_R(0) = (-\pi, \pi)$. Thus, the right-hand side of the above equation is zero and $\tilde{T}_{\vec{p}}$ is the same as $T_{\vec{p}}$ in 1D. As a result, we can compare this modified spectral approximation with the analytical expression (5.3) to see how well the low regularity of the integrand at the origin is treated. From Tables 1 and 2, we can see that the current approach produces a level of accuracy comparable with the non-uniform FFT approximation but is much faster than the latter.

It should be pointed out that $\tilde{T}_{\vec{p}}$ is different from $T_{\vec{p}}$ and $\tilde{T}_{\vec{p}}$ in multi-dimensions. The distributions of its entries are plotted in Fig. 5. One can see that they are slightly different from those in Fig. 4 for $\tilde{T}_{\vec{p}}$ but have the same asymptotic decay rate $|\vec{p}|^{-(d+1)/2}$ in 2D and 3D.

5.5 Summary of approximations of the stiffness matrix T

Properties of the four approximations for the stiffness matrix T are listed in Table 3. The FFT and non-uniform FFT approximations are based on the same stiffness matrix T defined in (5.1). The FFT approximation has good accuracy for large s (say, $s \geq 0.5$) but suffers from the low regularity of the integrand at the origin for small s . The non-uniform FFT approximation provides good accuracy for all $s \in (0, 1)$ (is less accurate than FFT for large s) but is expensive. The spectral and modified spectral approximations are fast and do not suffer from the low regularity of the integrand for small s but are based on different stiffness matrices, (5.11) and (5.22), respectively. These matrices have slower asymptotic decay rates than that of the stiffness matrix (5.1) except in 1D where (5.1) and (5.22) are the same.

6 Preconditioning

Recall that the linear algebraic system (2.7) can be solved efficiently with an iterative method although the coefficient matrix is dense. This is due mainly to the fact that I_h^{FD} is sparse and the multiplication of A_{FD} with vectors can be carried out efficiently using FFT. We consider preconditioning for the iterative solution of the linear system (2.7) to further improve the computational efficiency.

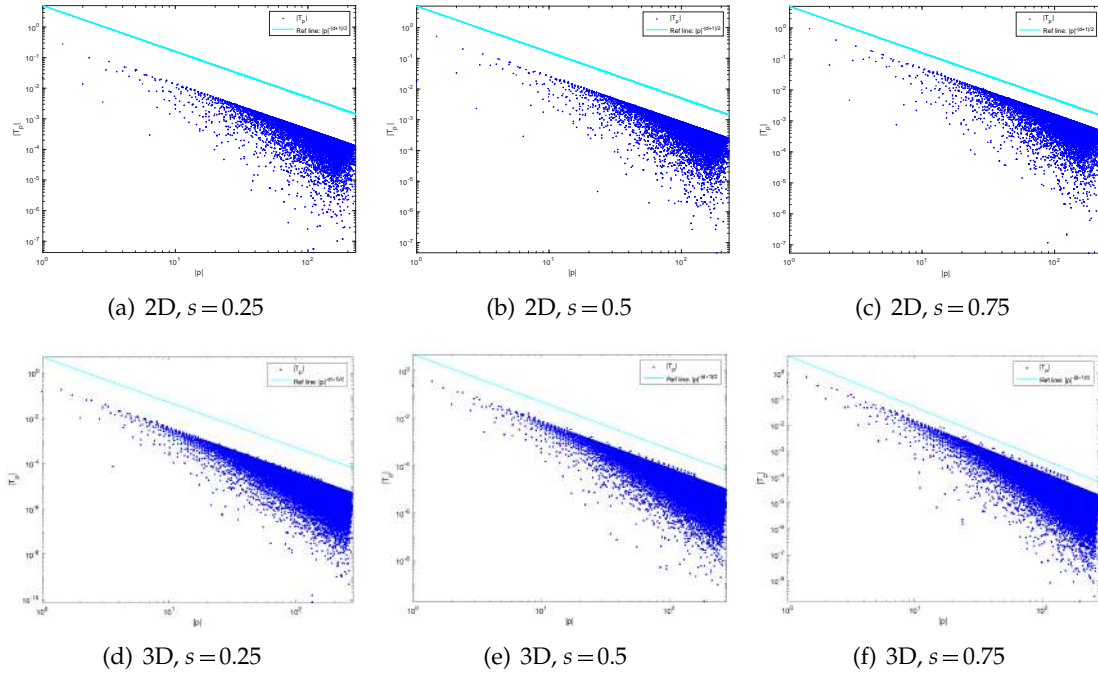


Figure 5: The decay of $\tilde{T}_{\vec{p}}$ as $|\vec{p}| \rightarrow \infty$ for $s = 0.25, 0.50$, and 0.75 . The reference line is $T_{\vec{p}} = |\vec{p}|^{-(d+1)/2}$ (for 2D and 3D).

Table 3: Summary of properties of the four approximations of the stiffness matrix. The preconditioning and solution of BVPs are tested with GoFD (cf. the linear system (2.7)). The accuracy of the FFT approximation is not good for small s . All four approximations lead to expected convergence order of GoFD for BVPs.

Approximation	T	How fast to compute	Asymptotic		Precond effective		Work for BVPs
			$d = 1$	$d \geq 2$	sparse	circulant	
FFT	(5.1)	fast	$\frac{1}{ \vec{p} ^{d+2s}}$		yes	yes	yes
non-uniform FFT	(5.1)	slow	$\frac{1}{ \vec{p} ^{d+2s}}$		yes	yes	yes
Spectral	(5.11)	fastest	$\frac{1}{ p ^{\min(2, 1+2s)}}$	$\frac{1}{ \vec{p} ^{(d+1)/2}}$	no	no	yes
Mod. Spectral	(5.22)	fast	$\frac{1}{ p ^{1+2s}}$	$\frac{1}{ \vec{p} ^{(d+1)/2}}$	no	yes	yes

A sparse preconditioner for solving (2.7) has been suggested in [28]. First, a sparsity pattern based on the FD discretization of the Laplacian is chosen. For example, 9-point and 27-point patterns can be taken in 2D and 3D, respectively. Then, a sparse matrix using the entries of A_{FD} at the positions specified by the pattern can be formed. Denote these matrices by $A_{\text{FD}}^{(9)}$ and $A_{\text{FD}}^{(27)}$, respectively. Next, define

$$A_h^{(9)} = (I_h^{\text{FD}})^T A_{\text{FD}}^{(9)} I_h^{\text{FD}}, \quad A_h^{(27)} = (I_h^{\text{FD}})^T A_{\text{FD}}^{(27)} I_h^{\text{FD}}. \quad (6.1)$$

Finally, the sparse preconditioner for (2.7) is obtained using the modified incomplete Cholesky decomposition of $A_h^{(9)}$ or $A_h^{(27)}$ with dropoff threshold 10^{-3} . Notice that the so-obtained preconditioner is sparse and can be computed and applied economically.

Next, we consider a different preconditioner that is based on circulant preconditioners for Toeplitz systems (see, e.g., [13, 14]). In principle, circulant preconditioners for Toeplitz systems can be applied directly to A_{FD} since A_{FD} is a block Toeplitz matrix with Toeplitz blocks. Here, we present a simple and explicit description based on (3.11). Recall that constructing a preconditioner for A_{FD} means finding a way to solve $u_{m,n}$'s for given $A_{\text{FD}}\vec{u}_{\text{FD}}$. Unfortunately, we cannot do this directly from (3.11) because the Fourier transforms there use $4N_{\text{FD}}$ sample points in each axial direction but only $2N_{\text{FD}}$ points in each axial direction are used for u . To avoid this difficulty, we reduce the number of sampling points to $2N_{\text{FD}}$ and define an approximation for A_{FD} as

$$(\tilde{A}_{\text{FD}}\vec{u}_{\text{FD}})_{(j,k)} = \frac{1}{(2N_{\text{FD}})^2} \sum_{p=-N_{\text{FD}}}^{N_{\text{FD}}-1} \sum_{q=-N_{\text{FD}}}^{N_{\text{FD}}-1} \check{T}_{p,q} \check{u}_{p,q} (-1)^{p+N_{\text{FD}}+q+N_{\text{FD}}} \cdot e^{\frac{i2\pi(p+N_{\text{FD}})(j+N_{\text{FD}})}{2N_{\text{FD}}} + \frac{i2\pi(q+N_{\text{FD}})(k+N_{\text{FD}})}{2N_{\text{FD}}}}, \quad -N_{\text{FD}} \leq j, k \leq N_{\text{FD}}, \quad (6.2)$$

where

$$\check{T}_{p,q} = \sum_{m=-N_{\text{FD}}}^{N_{\text{FD}}-1} \sum_{n=-N_{\text{FD}}}^{N_{\text{FD}}-1} T_{m,n} e^{-\frac{i2\pi(m+N_{\text{FD}})(p+N_{\text{FD}})}{2N_{\text{FD}}} - \frac{i2\pi(n+N_{\text{FD}})(q+N_{\text{FD}})}{2N_{\text{FD}}}}, \quad (6.3)$$

$$\check{u}_{p,q} = \sum_{m=-N_{\text{FD}}}^{N_{\text{FD}}-1} \sum_{n=-N_{\text{FD}}}^{N_{\text{FD}}-1} u_{m,n} e^{-\frac{i2\pi(m+N_{\text{FD}})(p+N_{\text{FD}})}{2N_{\text{FD}}} - \frac{i2\pi(n+N_{\text{FD}})(q+N_{\text{FD}})}{2N_{\text{FD}}}}. \quad (6.4)$$

We hope that \tilde{A}_{FD} is a good approximation of A_{FD} . Most importantly, using the discrete Fourier transform and its inverse we can find the inverse of \tilde{A}_{FD} as

$$(\tilde{A}_{\text{FD}}^{-1}\vec{v}_{\text{FD}})_{(j,k)} = \frac{1}{(2N_{\text{FD}})^2} \sum_{p=-N_{\text{FD}}}^{N_{\text{FD}}-1} \sum_{q=-N_{\text{FD}}}^{N_{\text{FD}}-1} \check{T}_{p,q}^{-1} \check{v}_{p,q} (-1)^{p+N_{\text{FD}}+q+N_{\text{FD}}} \cdot e^{\frac{i2\pi(p+N_{\text{FD}})(j+N_{\text{FD}})}{2N_{\text{FD}}} + \frac{i2\pi(q+N_{\text{FD}})(k+N_{\text{FD}})}{2N_{\text{FD}}}}, \quad -N_{\text{FD}} \leq j, k \leq N_{\text{FD}}, \quad (6.5)$$

where \check{T} is given in (6.3) and \check{v} is the discrete Fourier transform of v_h (which has a similar expression as (6.4)). The computation of $\tilde{A}_{\text{FD}}^{-1}\vec{v}_{\text{FD}}$ requires three FFT/inverse FFT, totaling $\mathcal{O}(N_{\text{FD}}^d \log(N_{\text{FD}}^d))$ flops (in d -dimensions).

Once we have obtained the preconditioner for A_{FD} , we can form the preconditioner for the coefficient matrix of (2.7). Notice that

$$((I_h^{\text{FD}})^T A_{\text{FD}} I_h^{\text{FD}})^{-1} = (I_h^{\text{FD}})^+ A_{\text{FD}}^{-1} ((I_h^{\text{FD}})^+)^T, \quad (6.6)$$

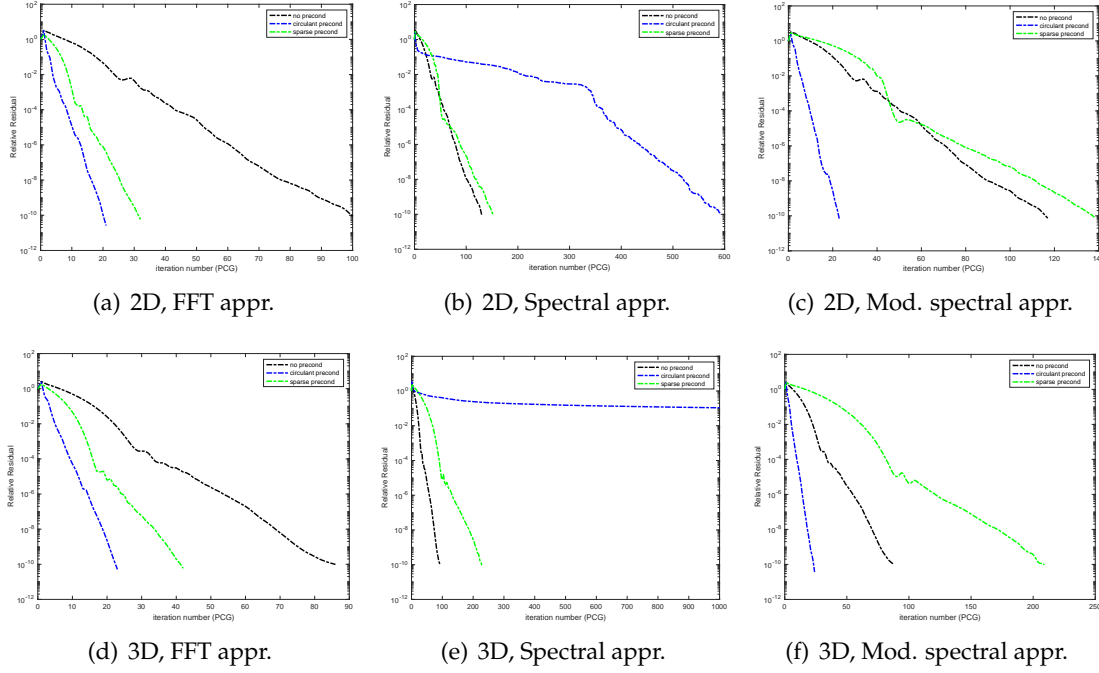


Figure 6: Example (1.4) with $s=0.75$ and in 2D and 3D. Convergence histories of PCG for solving (2.7) with $tol=10^{-10}$ for three different approximations of the stiffness matrix T . $M=2^{14}$, $n_G=64$, $N=11,930$ (for mesh \mathcal{T}_h), and $N_{FD}=75$ (for mesh \mathcal{T}_{FD}) are used in 2D and $M=2^{10}$, $n_G=64$, $N=922,447$ (for mesh \mathcal{T}_h), and $N_{FD}=110$ (for mesh \mathcal{T}_{FD}) are used in 3D.

where $(I_h^{FD})^+$ is the Moore-Penrose pseudo-inverse of I_h^{FD} ,

$$(I_h^{FD})^+ = (I_h^{FD})^T \left((I_h^{FD})^T I_h^{FD} \right)^{-1}. \quad (6.7)$$

The final circulant preconditioner for the system (2.7) is obtained by replacing A_{FD}^{-1} in (6.6) with \tilde{A}_{FD}^{-1} and $(I_h^{FD})^T I_h^{FD}$ in (6.7) with its modified incomplete Cholesky decomposition with dropoff threshold 10^{-3} .

Convergence histories of PCG for solving (2.7) are plotted in Fig. 6. It can be seen that for the FFT approximation of the stiffness matrix, both the sparse and circulant preconditioners perform well, significantly reducing the number of PCG iterations to reach a prescribed tolerance, with the latter doing slightly better than the former. For the spectral approximation, both preconditioners do not work, requiring more or much more iterations than CG without preconditioning. Recall that the spectral approximation uses a different stiffness matrix, (5.11), which has the different integrand and domain from (5.1). For the modified spectral approximation, the stiffness matrix is given in (5.22), which differs from (5.1) only by the integration domain. In this case, the circulant preconditioner works well as it does for the FFT approximation. This actually is the main motivation to

introduce the modified spectral approximation. Unfortunately, the sparse preconditioner still does not work for this case.

At this point, it remains unclear why both sparse and circulant preconditioners do not work for the spectral approximation. Understanding this and developing effective preconditioners for the spectral approximation is an interesting topic for future research.

7 Numerical examples

In this section we present numerical results obtained for Example (1.4) in 2D and 3D to demonstrate that GoFD with all four approximations for the stiffness matrix produces numerical solutions for BVP (1.1) with expected convergence order. In our computation, the linear system (2.7) is solved using PCG with the circulant preconditioner except for the spectral approximation when CG without preconditioning is used. We use $n_G = 64$ (in the spectral and modified spectral approximations) and $M = 2^{14}$ (for 2D) and $M = 2^{10}$ (for 3D) in the FFT and modified spectral approximations. Results obtained with the non-uniform FFT approximation are omitted here since they are almost identical to those obtained with the FFT approximation and these two approximations are based on the same stiffness matrix (5.1).

The L^2 norm of the error obtained with GoFD with quasi-uniform meshes is plotted as a function of N (the number of elements of mesh \mathcal{T}_h) in Figs. 7 and 8 for 2D and 3D, respectively. The results are almost identical for all three approximations for the stiffness matrix. Moreover, the error shows a expected convergence rate, $\mathcal{O}(\bar{h}^{\min(1, 0.5+s)})$, where $\bar{h} = N^{-1/d}$ is the average element diameter. These results show that GoFD works well for solving BVP (1.1) with all four approximations of the stiffness matrix.

Next, we consider adaptive meshes. It is known (see, e.g., [2, 39]) that the solution of (1.1) has low regularity near the boundary of Ω ,

$$u(\vec{x}) \sim \text{dist}^s(\vec{x}, \partial\Omega), \quad \text{for } \vec{x} \text{ close to } \partial\Omega,$$

where $\text{dist}(\vec{x}, \partial\Omega)$ denotes the distance from \vec{x} to the boundary of Ω . Mesh adaptation is useful to improve accuracy and convergence order. Here, we use the so-called moving mesh PDE (MMPDE) method [27] to generate an adaptive mesh based on the function $v(\vec{x}) = \text{dist}^s(\vec{x}, \partial\Omega)$. Once an adaptive mesh is generated, BVP (1.1) is solved using GoFD on the generated mesh. No iteration between mesh generation and BVP solution is taken. To save space, we do not give the description of the MMPDE method here. The interested reader is referred to [28, Section 4] and [27] for the detail of the method.

Typical adaptive meshes and computed solutions in 2D are shown in Fig. 9. It can be seen that mesh concentration is higher near the boundary. To save space, we present the error in Fig. 10 only for GoFD with the modified spectral approximation of the stiffness matrix. It is clear that the error converges at a second-order rate $\mathcal{O}(\bar{h}^2)$. It is also interesting to observe that for $s = 0.25$ and 0.5 , the error has a slower convergence rate before it reaches the second-order rate for finer meshes.

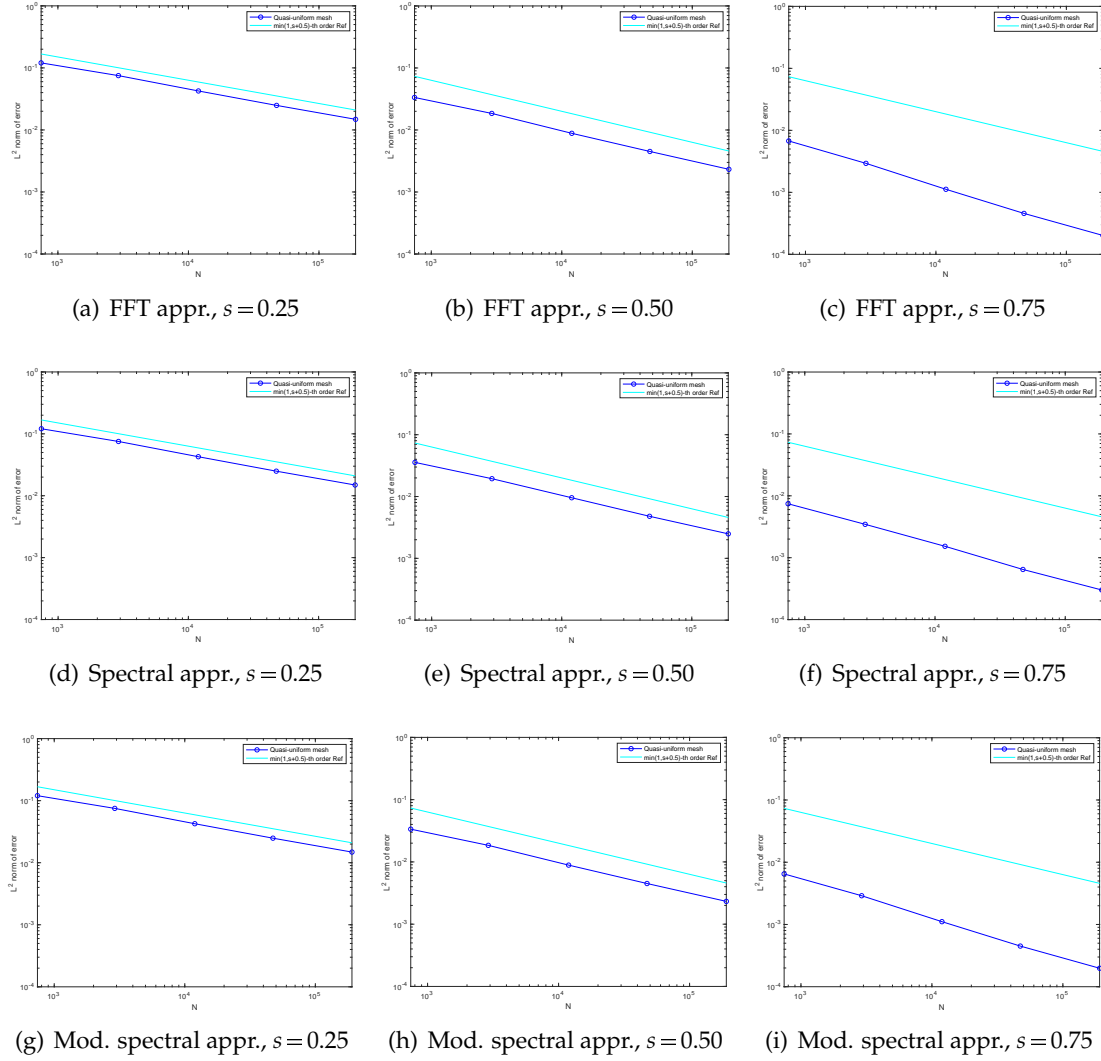


Figure 7: Example (1.4) in 2D. The L^2 norm of the error is plotted as a function N for GoFD with various approximations of the stiffness matrix.

We present 3D adaptive mesh results in Fig. 11. The error is smaller than those in Fig. 8 for quasi-uniform meshes but has not reached second order especially for $s = 0.25$ and 0.5 for the considered range of the mesh size. The computation with meshes of larger N runs out memory. For those cases, the minimum height a_{h_i} of the adaptive mesh is very small, requiring a very large N_{FD} (cf. (2.6)) and thus a large amount of memory. This reflects a drawback of GoFD with 3D adaptive meshes.

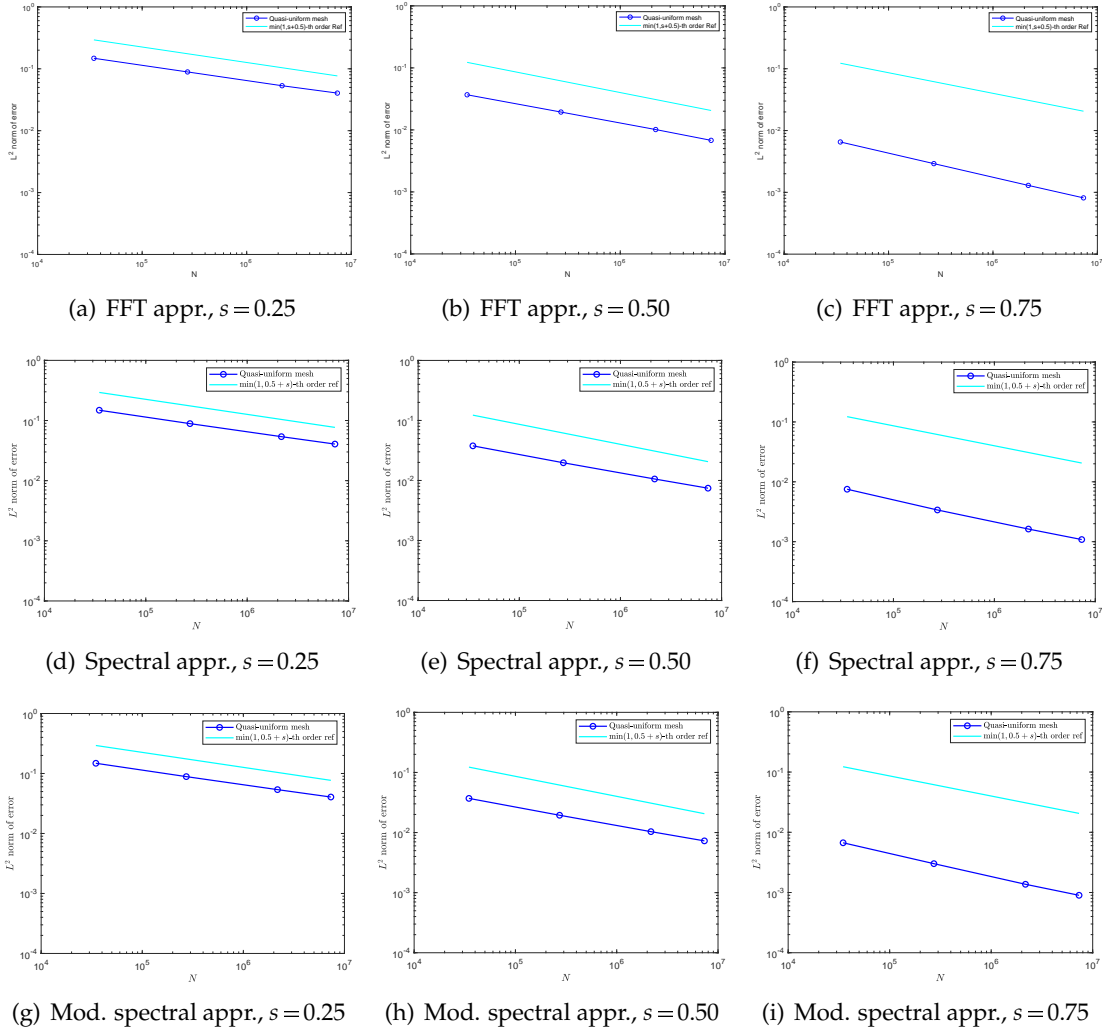


Figure 8: Example (1.4) in 3D. The L^2 norm of the error is plotted as a function N for GoFD with various approximations of the stiffness matrix.

8 Conclusions

In the previous sections we have presented an analysis on the effect of the accuracy in approximating the stiffness matrix T on the accuracy in the FD solution of BVP (1.1). The analysis and numerics show that this effect can be significant, requiring accurate and reasonably economic approximations to the stiffness matrix. Four approaches for approximating T have been discussed and shown to work well with GoFD for the numerical solution of BVP (1.1). Their properties are summarized in Table 3. This study shows that the FFT approach is a good choice for large s (say $s \geq 0.5$) since it is of high

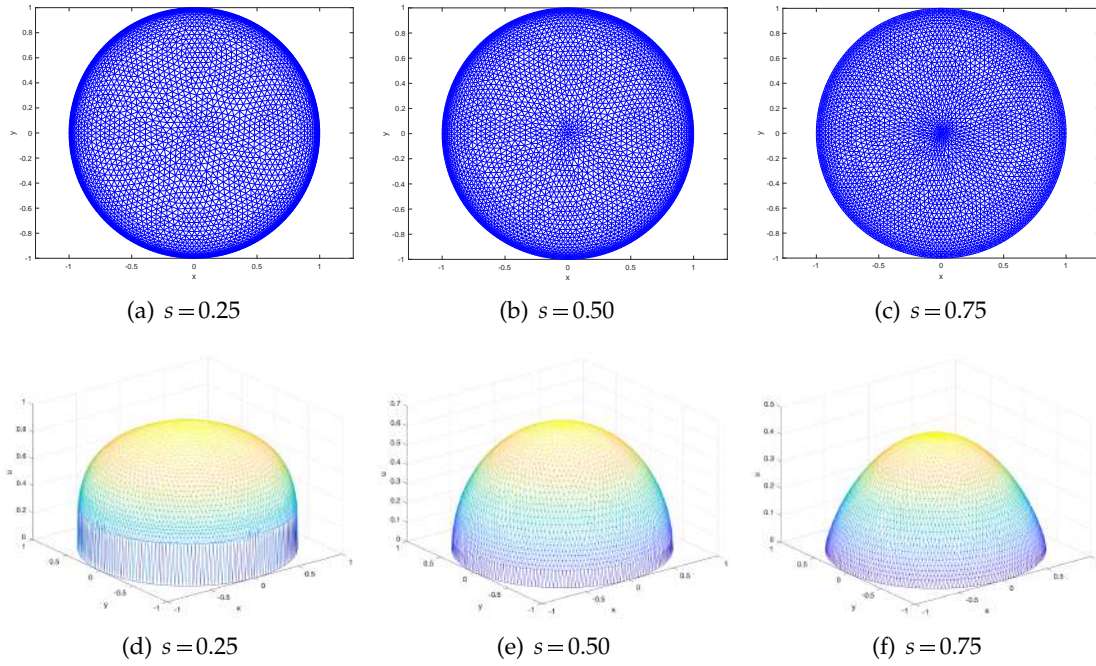


Figure 9: Example (1.4) in 2D. Adaptive meshes and computed solutions obtained with GoFD with the modified spectral approximation.

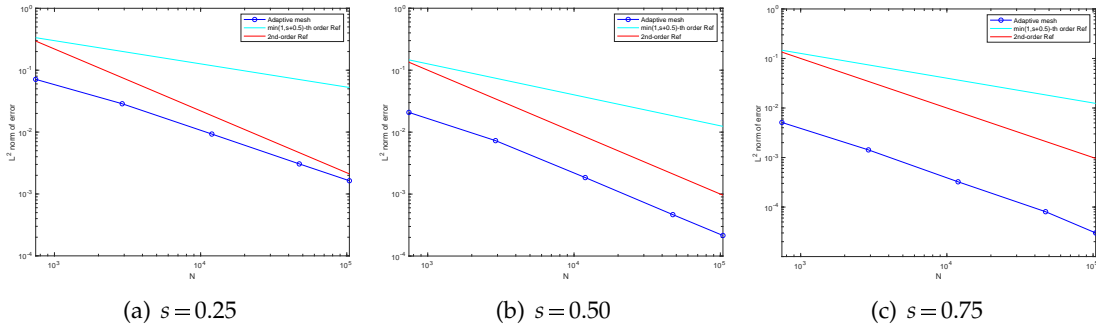


Figure 10: Example (1.4) in 2D. The L^2 norm of the error is plotted as a function N for GoFD with the modified spectral approximation for the stiffness matrix and adaptive meshes.

accuracy, has fast asymptotic decay rates away from the diagonal line, works well with both sparse and circulant preconditioners, and is reasonably economic to compute. For small s , the modified spectral approximation is a good choice since it leads to high accuracy, works well with the circulant preconditioner, and is reasonably economic to compute although it does not have an asymptotic decay as fast as those for the FFT approximation.

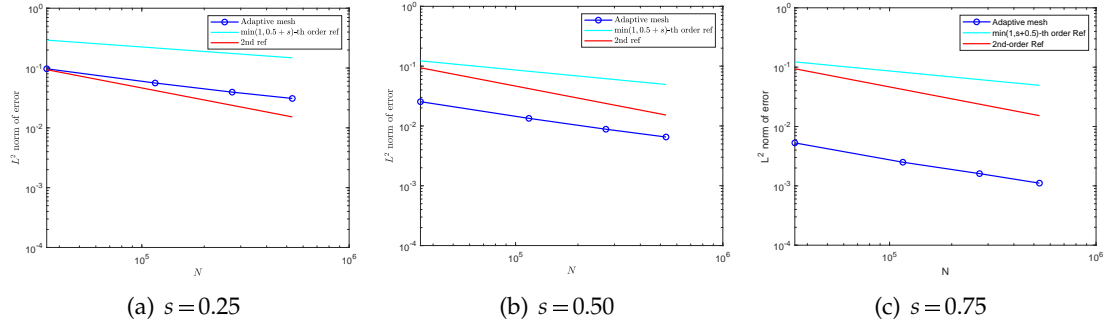


Figure 11: Example (1.4) in 3D. The L^2 norm of the error is plotted as a function N for GoFD with the modified spectral approximation for the stiffness matrix and adaptive meshes.

Acknowledgments

J. Shen was supported in part by the National Natural Science Foundation of China through grant [12101509] and the Sichuan Science and Technology Program through grant [2025ZNSFSC0811] and W. Huang was supported in part by the Simons Foundation through grant MP-TSM-00002397.

References

- [1] G. Acosta, F. M. Bersetche, and J. P. Borthagaray. A short FE implementation for a 2D homogeneous Dirichlet problem of a fractional Laplacian. *Comput. Math. Appl.*, 74:784–816, 2017.
- [2] G. Acosta and J. P. Borthagaray. A fractional Laplace equation: Regularity of solutions and finite element approximations. *SIAM J. Numer. Anal.*, 55:472–495, 2017.
- [3] M. Ainsworth and C. Glusa. Aspects of an adaptive finite element method for the fractional Laplacian: a priori and a posteriori error estimates, efficient implementation and multigrid solver. *Comput. Methods Appl. Mech. Engrg.*, 327:4–35, 2017.
- [4] M. Ainsworth and C. Glusa. Towards an efficient finite element method for the integral fractional Laplacian on polygonal domains. In *Contemporary Computational Mathematics—A Celebration of the 80th Birthday of Ian Sloan. Vol. 1, 2*, pages 17–57. Springer, Cham, 2018.
- [5] G. E. Andrews, R. Askey, and R. Roy. *Special Functions*, volume 71 of *Encyclopedia of Mathematics and its Applications*. Cambridge University Press, Cambridge, 1999.
- [6] H. Antil, T. Brown, R. Khatri, A. Onwunta, D. Verma, and M. Warma. Chapter 3 – Optimal control, numerics, and applications of fractional PDEs. *Handbook of Numerical Analysis*, 23:87–114, 2022.
- [7] H. Antil, P. Dondl, and L. Striet. Approximation of integral fractional Laplacian and fractional PDEs via sinc-basis. *SIAM J. Sci. Comput.*, 43:A2897–A2922, 2021.
- [8] A. H. Barnett. Aliasing error of the $\exp(\beta\sqrt{1-z^2})$ kernel in the nonuniform fast Fourier transform. *Appl. Comput. Harmon. Anal.* 51, 1-16, 2021.

- [9] A. H. Barnett, J. F. Magland, and L. af Klinteberg. A parallel non-uniform fast Fourier transform library based on an “exponential of semicircle” kernel. *SIAM J. Sci. Comput.*, 41, C479-C504, 2019.
- [10] A. Bonito and W. Lei. Approximation of the spectral fractional powers of the Laplace-Beltrami operator. *Numer. Math. Theor. Meth. Appl.*, 15:1193-1218, 2022.
- [11] A. Bonito, W. Lei, and J. E. Pasciak. Numerical approximation of the integral fractional Laplacian. *Numer. Math.*, 142:235–278, 2019.
- [12] J. Burkardt, Y. Wu, and Y. Zhang. A unified meshfree pseudospectral method for solving both classical and fractional PDEs. *SIAM J. Sci. Comput.*, 43:A1389–A1411, 2021.
- [13] R. H. Chan and M. K. Ng. Conjugate gradient methods for Toeplitz systems. *SIAM Rev.*, 38:427–482, 1996.
- [14] T. F. Chan. An optimal circulant preconditioner for Toeplitz systems. *SIAM J. Sci. Statist. Comput.*, 9:766–771, 1988.
- [15] M. D’Elia and M. Gulian. Analysis of anisotropic nonlocal diffusion models: Well-posedness of fractional problems for anomalous transport. *Numer. Math. Theor. Meth. Appl.*, 15:851-875, 2022.
- [16] N. Du, H.-W. Sun, and H. Wang. A preconditioned fast finite difference scheme for space-fractional diffusion equations in convex domains. *Comput. Appl. Math.*, 38:Paper No. 14, 13, 2019.
- [17] Q. Du, L. Ju, and J. Lu. A discontinuous Galerkin method for one-dimensional time-dependent nonlocal diffusion problems. *Math. Comp.*, 88:123–147, 2019.
- [18] S. Duo, H. W. van Wyk, and Y. Zhang. A novel and accurate finite difference method for the fractional Laplacian and the fractional Poisson problem. *J. Comput. Phys.*, 355:233–252, 2018.
- [19] S. Duo and Y. Zhang. Computing the ground and first excited states of the fractional Schrödinger equation in an infinite potential well. *Commun. Comput. Phys.*, 18:321–350, 2015.
- [20] A. Dutt and V. Rokhlin. Fast Fourier transforms for nonequispaced data. *SIAM J. Sci. Comput.*, 14:1368–1393, 1993.
- [21] B. Dyda, A. Kuznetsov, and M. Kwaśnicki. Fractional Laplace operator and Meijer G-function. *Constr. Approx.*, 45:427–448, 2017.
- [22] M. Faustmann, M. Karkulik, and J. M. Melenk. Local convergence of the FEM for the integral fractional Laplacian. *SIAM J. Numer. Anal.*, 60:1055–1082, 2022.
- [23] L. N. G. Filon. On a quadrature formula for trigonometric integrals. *Model. Anal. Inf. Syst.*, 49:38–47, 1928.
- [24] I. S. Gradshteyn and I. M. Ryzhik. *Table of Integrals, Series, and Products*. Elsevier/Academic Press, Amsterdam, eighth edition, 2015. Translated from the Russian, Translation edited and with a preface by Daniel Zwillinger and Victor Moll.
- [25] Z. Hao, M. Park, and Z. Cai. Neural network method for integral fractional Laplace equations. *East Asian J. Appl. Math.*, 13:95-118, 2023.
- [26] Z. Hao, Z. Zhang, and R. Du. Fractional centered difference scheme for high-dimensional integral fractional Laplacian. *J. Comput. Phys.*, 424:Paper No. 109851, 17, 2021.
- [27] W. Huang and R. D. Russell. *Adaptive Moving Mesh Methods*. Springer, New York, 2011. Applied Mathematical Sciences Series, Vol. 174.
- [28] W. Huang and J. Shen. A grid-overlay finite difference method for the fractional Laplacian on arbitrary bounded domains. *SIAM J. Sci. Comput.*, 46:A744–A769, 2024.
- [29] W. Huang and J. Shen. A grid-overlay finite difference method for inhomogeneous Dirichlet problems of the fractional Laplacian on arbitrary bounded domains. *J. Sci. Comput.*, 102:Paper No. 50, 2025.

- [30] Y. Huang and A. Oberman. Numerical methods for the fractional Laplacian: A finite difference-quadrature approach. *SIAM J. Numer. Anal.*, 52:3056–3084, 2014.
- [31] Y. Huang and A. Oberman. Finite difference methods for fractional Laplacians. *arXiv:1611.00164*, 2016.
- [32] H. Li, R. Liu, and L.-L. Wang. Efficient hermite spectral-Galerkin methods for nonlocal diffusion equations in unbounded domains. *Numer. Math. Theory Methods Appl.*, 15:1009–1040, 2022.
- [33] A. Lischke, G. Pang, M. Gulian, and et al. What is the fractional Laplacian? A comparative review with new results. *J. Comput. Phys.*, 404:109009, 62, 2020.
- [34] V. Minden and L. Ying. A simple solver for the fractional Laplacian in multiple dimensions. *SIAM J. Sci. Comput.*, 42:A878–A900, 2020.
- [35] M. D. Ortigueira. Fractional central differences and derivatives. *J. Vib. Control*, 14:1255–1266, 2008.
- [36] G. Pang, W. Chen, and Z. Fu. Space-fractional advection-dispersion equations by the Kansa method. *J. Comput. Phys.*, 293:280–296, 2015.
- [37] H.-K. Pang and H.-W. Sun. Multigrid method for fractional diffusion equations. *J. Comput. Phys.*, 231:693–703, 2012.
- [38] A. P. Prudnikov, Y. A. Brychkov, and O. I. Marichev. *Integrals and Series. Vol. 2.* Gordon & Breach Science Publishers, New York, second edition, 1988. Special functions, Translated from the Russian by N. M. Queen.
- [39] X. Ros-Oton and J. Serra. The Dirichlet problem for the fractional Laplacian: Regularity up to the boundary. *J. Math. Pures Appl.*, 101:275–302, 2014.
- [40] J. Shen, B. Shi, and W. Huang. Meshfree finite difference solution of homogeneous Dirichlet problems of the fractional Laplacian. *Comm. Appl. Math. Comp.*, 2024, <https://doi.org/10.1007/s42967-024-00368-z>.
- [41] F. Song, C. Xu, and G. E. Karniadakis. Computing fractional Laplacians on complex-geometry domains: Algorithms and simulations. *SIAM J. Sci. Comput.*, 39:A1320–A1344, 2017.
- [42] J. Sun, W. Deng, and D. Nie. Finite difference method for inhomogeneous fractional Dirichlet problem. *Numer. Math. Theor. Meth. Appl.*, 15:744–767, 2022.
- [43] J. Sun, D. Nie, and W. Deng. Algorithm implementation and numerical analysis for the two-dimensional tempered fractional Laplacian. *BIT*, 61:1421–1452, 2021.
- [44] X. Tian and Q. Du. Analysis and comparison of different approximations to nonlocal diffusion and linear peridynamic equations. *SIAM J. Numer. Anal.*, 51:3458–3482, 2013.
- [45] H. Wang and T. S. Basu. A fast finite difference method for two-dimensional space-fractional diffusion equations. *SIAM J. Sci. Comput.*, 34:A2444–A2458, 2012.
- [46] W. Zhang, J. Yang, J. Zhang, and Q. Du. Artificial boundary conditions for nonlocal heat equations on unbounded domain. *Commun. Comput. Phys.*, 21:16–39, 2017.
- [47] S. Zhou and Y. Zhang. A novel and simple spectral method for nonlocal PDEs with the fractional Laplacian. *Comput. Math. Appl.*, 168:133–147, 2024.